Analytical Evaluation of Ballasted Track Substructure Response under Repeated Train Loads

Piyush Punetha[1], Sanjay Nimbalkar, [Ph.D MIEAust CPEng NER 2✉], Hadi Khabbaz, [Ph.D.3]

ABSTRACT: The irrecoverable deformations in the substructure layers are detrimental to the track stability and demand frequent maintenance. With an escalation in axle-load and traffic volume, the frequency of maintenance operations has remarkably increased. Consequently, there is an inevitable need to predict the long-term behavior of the track substructure layers. This article presents a methodology to evaluate the recoverable and irrecoverable responses of the substructure layers under the train-induced repetitive loads. The present method utilizes an integrated approach combining track loading, resiliency and settlement models. The track substructure layers are simulated as lumped masses that are connected by springs and dashpots. The method is successfully validated against the field investigation data reported in the literature. A parametric study is conducted to investigate the influence of substructure layer properties on the track response. The results reveal that the response of each track layer is significantly influenced by the neighboring layer properties and the incorporation of multi-layered track structure enables more accurate prediction of track behavior. The present analytical approach is simple, computationally efficient and may assist the practicing engineers in the safer design of the ballasted track.

Keywords: Railway track; Substructure; Mathematical model; Resiliency**;** Irrecoverable deformation.

[1] PhD candidate, School of Civil and Environmental Engineering, FEIT, University of Technology Sydney, NSW-2007, Australia. Email: Piyush.Punetha@student.uts.edu.au, ORCID: 0000-0002-0812-4708.
[2] Senior Lecturer, School of Civil and Environmental Engineering, FEIT, University of Technology Sydney, NSW-2007, Australia. Email: Sanjay.Nimbalkar@uts.edu.au, ORCID: 0000-0002-1538-3396.
[3] Associate Professor, School of Civil and Environmental Engineering, FEIT, University of Technology Sydney, NSW-2007, Australia. Email: Hadi.Khabbaz@uts.edu.au, ORCID: 0000-0001-6637-4601.
✉ Corresponding author

INTRODUCTION

The ballasted railway track is a complex engineering structure that consists of two primary components: substructure and superstructure. The substructure comprises of ballast, capping (subballast), structural fill, general fill and subgrade layers whose behavior governs the track performance and maintenance requirements (Selig and Waters 1994). These substructure layers undergo resilient (elastic) as well as irrecoverable deformation under the application of train induced repeated loads. The differential settlement produced due to non-uniform irrecoverable deformation in these layers is detrimental for track stability as it demands frequent maintenance cycles, increases the dynamic wheel-rail interactions and leads to poor riding quality (Esveld 2001).

A hike in traffic volume, speed and axle loads on railway tracks has increased the stresses and deformations in the substructure layers (Nimbalkar and Indraratna 2016; Priest et al. 2010). Consequently, the frequency of maintenance cycles has increased to meet this ever-increasing demand. These maintenance operations require substantial financial investments due to the lack of proper planning and poor diagnosis of the track geometry degradation problems (Nguyen et al. 2016). Therefore, the accurate prediction of the behavior of individual track layers is imperative to plan and reduce the frequency of maintenance operations.

The field investigations are essential tools to understand the behavior of individual substructure layers and their mutual interaction. However, these studies are time-consuming and costly. The numerical and analytical approaches offer cost-effective alternatives to understand the behavior of the substructure layers. Several researchers have attempted to predict the track response using 2D (e.g. Kuo and Huang 2009; Yang et al. 2009), 2.5 D (e.g. Costa et al. 2010; Galvín et al. 2018; Hung et al. 2013; Yang and Hung 2001) and 3D finite element (FE) analyses (e.g. Banimahd et al. 2013; Bian et al. 2010; Chen and Zhou 2018; Connolly et al. 2013; Galvín et al. 2010; Hall 2003; Li et al. 2018; Sayeed and Shahin 2016;

Shahu et al. 1999; Stewart and Selig 1982). Although the 2D models may be appropriate for predicting the static response of the track, these models cannot accurately simulate the three-dimensional loading due to train-traffic (Powrie et al. 2007). On the other hand, 3D modelling of railway tracks using the FE method may be computationally intensive and time-consuming (Karlström and Boström 2006).

In contrast to FE analyses, analytical techniques are comparatively faster and may also facilitate the interpretation of results obtained from the FE analyses. Therefore, several analytical models have been developed to predict the behavior of the railway tracks under train induced repeated loading. These models range from a simple beam on elastic foundation (BoEF) approach (Esveld 2001) to advanced 3D vehicle-track coupled models (e.g. Guo and Zhai 2018; Zhai et al. 2009). Usually, the substructure in analytical models is either represented using equivalent springs and/or dashpots (Basu and Kameswara Rao 2013; Chen and Huang 2000), as a homogenous or multilayered half-space (Dieterman and Metrikine 1997; Kaynia et al. 2000; Metrikine and Popp 1999; Takemiya and Bian 2005) or a combination of multilayered half-space, springs and/or dashpots (Sheng et al. 1999). The representation of substructure as an equivalent spring may predict the overall track response, however, it neglects the mutual interaction between the substructure layers. A few researchers represented the ballast and/or capping layers as individual masses connected by springs and dashpots (Sun and Dhanasekar 2002; Zhai et al. 2004). Choudhury et al. (2008) employed a two-degree of freedom mass-spring-dashpot model to study the response of different subgrade soils below a railway track under cyclic loading condition. However, their approach neglected the role of capping in the track response and also ignored the continuity of the substructure layers along the longitudinal direction (i.e., the direction of train movement). Nevertheless, a limited number of approaches have captured the irrecoverable deformation in the individual substructure layers under train-induced repeated loads.

This paper presents a methodology to evaluate both the resilient and irrecoverable responses of the track substructure layers under train-induced repetitive loads. The resilient response is evaluated by modelling the substructure layers as lumped masses connected by springs and dashpots. The irrecoverable response is evaluated using the empirical settlement models for ballast, capping and subgrade. The present model provides an insight into the deformation of the individual substructure layers, their mutual interaction and the influence of substructure layer properties on track response. The accuracy of the present method is validated by comparing the predicted results against the field investigation data reported in the literature. The present methodology is simple, computationally efficient and can readily be used to predict the cumulative track deformations. Consequently, the long term performance of the tracks can be evaluated.

METHODOLOGY FOR PREDICTION OF TRACK SETTLEMENT

The present study employs an integrated approach which combines three models as illustrated below:

- Track loading model: this model evaluates the train-induced repetitive loads that act on the top of the ballast layer.
- Track resiliency model: this model determines the resilient response of the track layers to the repeated train loading in terms of displacement, velocity and acceleration time histories.
- Track settlement model: this model evaluates the cumulative settlement in the substructure layers due to repeated passage of trains.

Track loading model

In the ballasted railway tracks, the train-induced repetitive loads are transferred to the substructure layers through the sleeper-ballast contact. The sleeper-ballast contact force at each

sleeper location varies with time during the train passage. This force can be evaluated by using the beam on elastic foundation (BoEF) method. In this approach, the railway track is considered as a Euler-Bernoulli beam resting on an elastic foundation and the governing differential equation for the displacement of the beam is given by (Esveld 2001):

$$E_{\mathrm{r}} I \frac{d^4\delta(x)}{dx^4} + k\delta(x) = 0 \tag{1}$$

where E_{r} and I are Young's modulus (N/m^2) and the moment of inertia of the rail (m^4), respectively; k denotes the track modulus (N/m^2); $\delta(x)$ is the vertical track deflection (m) at a distance 'x' (m) along the longitudinal direction as shown in Fig. 1. The vertical deflection due to a static wheel load Q (N) (located at x = 0) can be evaluated by solving Eq. (1) under the boundary conditions $\delta(\infty) = 0$, $\delta'(0) = 0$ and $\delta'''(0) = Q/(2E_{\mathrm{r}}I)$ as:

$$\delta(x) = \frac{Q}{2kL} e^{-\left(\frac{x}{L}\right)} \left[\cos\left(\frac{x}{L}\right) + \sin\left(\frac{x}{L}\right)\right] \tag{2}$$

where L is the characteristic length (m) [$L = (4E_{\mathrm{r}}I/k)^{1/4}$]. The term $k\delta(x)$ in Eq. (1) represents the reaction force per unit length provided by the track to the rail. Since the rail is supported at discrete locations by the sleepers, the reaction force provided by each rail seat (i.e., the rail seat load) can be calculated by multiplying $k\delta(x)$ with the sleeper spacing [S (m)].

As the beam on elastic foundation (BoEF) approach [Eq. (2)] considers the downward deflection to occur within a distance of -3πL/4 to 3πL/4 from the point of load application (Esveld 2001), the rail seat load at a particular time instant due to a single wheel can be calculated for all sleepers lying within this range. Subsequently, the variation of rail seat load [$Q_{\mathrm{r,n}}(t)$] with time due to the cumulative train loading can be calculated using the superposition principle as:

$$Q_{\mathrm{r,n}}(t) = Sk \sum_{j=1}^{a_{\mathrm{t}}} \delta(x_{\mathrm{nj}}, t) \tag{3}$$

where $Q_{r,n}$ (t) is the total rail seat load (N) at n^{th} sleeper at time t (i.e. sleeper–ballast contact force); a_t denotes the total number of wheels/axles under consideration; x_{nj} is the distance (m) between the n^{th} sleeper and j^{th} wheel/axle. Fig. 1 illustrates an example to calculate the rail seat load-time history at a sleeper due to the passage of Thalys high-speed train travelling at a speed of 100 km/h. Thalys high-speed train operates on the European high-speed rail corridor with a maximum speed of 300 km/h. It is assumed that the rail and the wheels are free from defects and the subgrade is stiff. A stiff subgrade is usually characterized by a high value of elastic modulus (69–138 MPa) and high compressive strength (207–345 kPa) (Li et al. 2016).

Fig. 1(a) shows the configuration of the Thalys high-speed train. It comprises of two locomotives and eight carriages that are supported by two-axle bogies. The total number of axles on the train is 26. It is assumed that the train is moving in the positive x-direction. Referring to Fig. 1(b), at time instant t_1, the n^{th} sleeper is at a distance of x_{n1} (t_1) and x_{n2} (t_1) from the leading (Q_1) and trailing wheel (Q_2), respectively. The distribution of rail deflection due to each wheel load, calculated using Eq. (2), is also shown in Fig. 1(b). It is apparent from the figure that the trailing wheel does not contribute to the deflection at the n^{th} sleeper at time t_1, since x_{n2} (t_1) is greater than $3\pi L/4$. As the train moves forward, the total deflection at the n^{th} sleeper at time t_2 is the sum of deflection due to both the wheels [refer to Fig. 1(c)]. Similarly, the deflection due to other wheel loads can be calculated at each time instant. Subsequently, the rail seat load-time history is calculated using Eq. (3) at all the sleeper locations by applying a time shift according to the axle spacing and train speed. Fig. 1(d) shows the resulting rail-seat load time history at the n^{th} and n^{th}+1 sleeper (i.e. next to n^{th} sleeper) due to a single passage of Thalys train at a speed of 100 km/h. It can be observed that a time lag exists in the load time history for the n^{th}+1 sleeper. This time lag is equal to S/V, where, V represents the train speed (m/s).

Track resiliency model

The dynamic response of the railway track to train-induced repetitive loads is simulated using a three degree of freedom mass-spring-dashpot (3DoF MSD) model. Fig. 2 shows the MSD model for the dynamic analysis of the track. The track structure is assumed to be symmetric with respect to the track centerline. The ballast, capping, and subgrade layers are represented as lumped masses that are connected by springs and dashpots. The subgrade layer overlays the bedrock. The motion of the track layers is considered only in the vertical direction. The ballast-capping and capping-subgrade interfaces are assumed to be rigid, i.e., a no-slip condition exists for these interfaces. Zhai et al. (2004) used shear springs and dashpots between adjacent ballast masses to account for the continuity along the longitudinal direction. This approach of employing shear springs and dashpots has been extended to the capping and subgrade masses in the present method.

Equations of motion

Considering the dynamic equilibrium of the system below n^{th} sleeper (refer to Fig. 2), the following system of equations can be derived using the D'Alembert's principle:

$$m_{\mathrm{s}}\ddot{y}_{\mathrm{s,n}}(t) + c_{\mathrm{s}}\dot{y}_{\mathrm{s,n}}(t) + c_{\mathrm{c}}\left[\dot{y}_{\mathrm{s,n}}(t) - \dot{y}_{\mathrm{c,n}}(t)\right] + k_{\mathrm{s}}y_{\mathrm{s,n}}(t) + k_{\mathrm{c}}\left[y_{\mathrm{s,n}}(t) - y_{\mathrm{c,n}}(t)\right] + k_{\mathrm{s}}^{s}\left[2y_{\mathrm{s,n}}(t) - y_{\mathrm{s,n+1}}(t) - y_{\mathrm{s,n-1}}(t)\right] + c_{\mathrm{s}}^{s}\left[2\dot{y}_{\mathrm{s,n}}(t) - \dot{y}_{\mathrm{s,n+1}}(t) - \dot{y}_{\mathrm{s,n-1}}(t)\right] = f_{\mathrm{s,n}}(t) \quad (4a)$$

$$m_{\mathrm{c}}\ddot{y}_{\mathrm{c,n}}(t) + c_{\mathrm{c}}[\dot{y}_{\mathrm{c,n}}(t) - \dot{y}_{\mathrm{s,n}}(t)] + c_{\mathrm{b}}\left[\dot{y}_{\mathrm{c,n}}(t) - \dot{y}_{\mathrm{b,n}}(t)\right] + k_{\mathrm{c}}[y_{\mathrm{c,n}}(t) - y_{\mathrm{s,n}}(t)] + k_{\mathrm{b}}\left[y_{\mathrm{c,n}}(t) - y_{\mathrm{b,n}}(t)\right] + k_{\mathrm{c}}^{s}\left[2y_{\mathrm{c,n}}(t) - y_{\mathrm{c,n+1}}(t) - y_{\mathrm{c,n-1}}(t)\right] + c_{\mathrm{c}}^{s}\left[2\dot{y}_{\mathrm{c,n}}(t) - \dot{y}_{\mathrm{c,n+1}}(t) - \dot{y}_{\mathrm{c,n-1}}(t)\right] = f_{\mathrm{c,n}}(t) \quad (4b)$$

$$m_{\mathrm{b}}\ddot{y}_{\mathrm{b,n}}(t) + c_{\mathrm{b}}\left[\dot{y}_{\mathrm{b,n}}(t) - \dot{y}_{\mathrm{c,n}}(t)\right] + k_{\mathrm{b}}\left[y_{\mathrm{b,n}}(t) - y_{\mathrm{c,n}}(t)\right] + k_{\mathrm{b}}^{s}\left[2y_{\mathrm{b,n}}(t) - y_{\mathrm{b,n+1}}(t) - y_{\mathrm{b,n-1}}(t)\right] + c_{\mathrm{b}}^{s}\left[2\dot{y}_{\mathrm{b,n}}(t) - \dot{y}_{\mathrm{b,n+1}}(t) - \dot{y}_{\mathrm{b,n-1}}(t)\right] = f_{\mathrm{b,n}}(t) \quad (4c)$$

where the subscripts 'b', 'c' and 's' denote the ballast, capping and subgrade layers, respectively; subscripts 'n', 'n-1' and 'n+1' represent the n^{th}, previous and next to n^{th} sleeper, respectively; m, c and k represent the vibrating mass (kg), damping coefficient (Ns/m) and

stiffness (N/m), respectively; k^s and c^s are the shear stiffness (N/m) and shear damping coefficients (Ns/m); $f(t)$, $\ddot{y}(t)$, $\dot{y}(t)$ and $y(t)$ denote the external force (N), vertical acceleration (m/s^2), velocity (m/s) and displacement (m), respectively. Eqs. [4(a–c)] can be further simplified as:

$$\begin{bmatrix} m_\mathrm{s} & 0 & 0 \\ 0 & m_\mathrm{c} & 0 \\ 0 & 0 & m_\mathrm{b} \end{bmatrix} \begin{Bmatrix} \ddot{y}_{\mathrm{s,n}}(t) \\ \ddot{y}_{\mathrm{c,n}}(t) \\ \ddot{y}_{\mathrm{b,n}}(t) \end{Bmatrix} + \begin{bmatrix} c_\mathrm{s} + c_\mathrm{c} + 2c_\mathrm{s}^s & -c_\mathrm{c} & 0 \\ -c_\mathrm{c} & c_\mathrm{c} + c_\mathrm{b} + 2c_\mathrm{c}^s & -c_\mathrm{b} \\ 0 & -c_\mathrm{b} & c_\mathrm{b} + 2c_\mathrm{b}^s \end{bmatrix} \begin{Bmatrix} \dot{y}_{\mathrm{s,n}}(t) \\ \dot{y}_{\mathrm{c,n}}(t) \\ \dot{y}_{\mathrm{b,n}}(t) \end{Bmatrix}$$

$$+ \begin{bmatrix} k_\mathrm{s} + k_\mathrm{c} + 2k_\mathrm{s}^s & -k_\mathrm{c} & 0 \\ -k_\mathrm{c} & k_\mathrm{c} + k_\mathrm{b} + 2k_\mathrm{c}^s & -k_\mathrm{b} \\ 0 & -k_\mathrm{b} & k_\mathrm{b} + 2k_\mathrm{b}^s \end{bmatrix} \begin{Bmatrix} y_{\mathrm{s,n}}(t) \\ y_{\mathrm{c,n}}(t) \\ y_{\mathrm{b,n}}(t) \end{Bmatrix} = \begin{Bmatrix} f_{\mathrm{s,n}}(t) \\ f_{\mathrm{c,n}}(t) \\ f_{\mathrm{b,n}}(t) \end{Bmatrix}$$

$$+ \begin{bmatrix} c_\mathrm{s}^s & 0 & 0 \\ 0 & c_\mathrm{c}^s & 0 \\ 0 & 0 & c_\mathrm{b}^s \end{bmatrix} \begin{Bmatrix} \dot{y}_{\mathrm{s,n+1}}(t) + \dot{y}_{\mathrm{s,n-1}}(t) \\ \dot{y}_{\mathrm{c,n+1}}(t) + \dot{y}_{\mathrm{c,n-1}}(t) \\ \dot{y}_{\mathrm{b,n+1}}(t) + \dot{y}_{\mathrm{b,n-1}}(t) \end{Bmatrix} + \begin{bmatrix} k_\mathrm{s}^s & 0 & 0 \\ 0 & k_\mathrm{c}^s & 0 \\ 0 & 0 & k_\mathrm{b}^s \end{bmatrix} \begin{Bmatrix} y_{\mathrm{s,n+1}}(t) + y_{\mathrm{s,n-1}}(t) \\ y_{\mathrm{c,n+1}}(t) + y_{\mathrm{c,n-1}}(t) \\ y_{\mathrm{b,n+1}}(t) + y_{\mathrm{b,n-1}}(t) \end{Bmatrix} \quad (5)$$

Eq. (5) is solved using the Newmark's-β numerical integration scheme. The solution of the equation gives the transient displacement, velocity and acceleration response for the ballast, capping and subgrade layers. The time step in the present study is chosen as 1×10^{-4} s to achieve the desired accuracy.

Determination of model parameters

The input parameters include the mass, stiffness and damping coefficient of the ballast, capping and subgrade layers. To determine these parameters, a pyramidal distribution of vertical load from the sleeper to the substructure layers is assumed (Ahlbeck et al. 1975), which was found to be in close agreement with the field measurements (Zhang et al. 2016). In this model, the vertical stresses in the substructure layers are uniformly distributed within the pyramid and zero outside the pyramid. Thus, the portion inside the load distribution pyramid can be considered as the effective region of ballast, capping and subgrade in the dynamic analysis. Consequently, the mass and stiffness of the effective regions of substructure layers below each sleeper can be determined using the geometry of the pyramid as:

$$m_{\mathrm{b}} = \rho_{\mathrm{b}} h_b \left[l_{\mathrm{e}} b_{\mathrm{sl}} + (l_{\mathrm{e}} + b_{\mathrm{sl}}) h_{\mathrm{b}} \tan\alpha + \frac{4}{3} h_{\mathrm{b}}^2 \tan^2\alpha \right] \tag{6}$$

$$m_{\mathrm{c}} = \rho_{\mathrm{c}} h_c \left[l_{\mathrm{e}} b_{\mathrm{sl}} + (l_{\mathrm{e}} + b_{\mathrm{sl}})(2h_{\mathrm{b}} \tan\alpha + h_{\mathrm{c}} \tan\beta) + 4h_{\mathrm{b}} \tan\alpha \, (h_{\mathrm{b}} \tan\alpha + h_{\mathrm{c}} \tan\beta) + \frac{4}{3} h_{\mathrm{c}}^2 \tan^2\beta \right] \tag{7}$$

$$m_{\mathrm{s}} = \rho_{\mathrm{s}} h_s \left[l_{\mathrm{e}} b_{\mathrm{sl}} + (l_{\mathrm{e}} + b_{\mathrm{sl}})(2h_{\mathrm{b}} \tan\alpha + 2h_{\mathrm{c}} \tan\beta + h_{\mathrm{s}} \tan\gamma) + 4(h_{\mathrm{b}} \tan\alpha + h_{\mathrm{c}} \tan\beta)(h_{\mathrm{b}} \tan\alpha + h_{\mathrm{c}} \tan\beta + h_{\mathrm{s}} \tan\gamma) + \frac{4}{3} h_{\mathrm{s}}^2 \tan^2\gamma \right] \tag{8}$$

$$k_{\mathrm{b}} = \frac{2(l_{\mathrm{e}} - b_{\mathrm{sl}}) \tan\alpha}{\ln\left(\frac{l_{\mathrm{e}}}{b_{\mathrm{sl}}} \cdot \frac{b_{\mathrm{sl}} + 2h_{\mathrm{b}} \tan\alpha}{l_{\mathrm{e}} + 2h_{\mathrm{b}} \tan\alpha} \right)} E_{\mathrm{b}} \tag{9}$$

$$k_{\mathrm{c}} = \frac{2(l_{\mathrm{e}} - b_{\mathrm{sl}}) \tan\beta}{\ln\left(\frac{l_{\mathrm{e}} + 2h_{\mathrm{b}} \tan\alpha}{b_{\mathrm{sl}} + 2h_{\mathrm{b}} \tan\alpha} \cdot \frac{b_{\mathrm{sl}} + 2h_{\mathrm{b}} \tan\alpha + 2h_{\mathrm{c}} \tan\beta}{l_{\mathrm{e}} + 2h_{\mathrm{b}} \tan\alpha + 2h_{\mathrm{c}} \tan\beta} \right)} E_{\mathrm{c}} \tag{10}$$

$$k_{\mathrm{s}} = \frac{2(l_{\mathrm{e}} - b_{\mathrm{sl}}) \tan\gamma}{\ln\left(\frac{l_{\mathrm{e}} + 2h_{\mathrm{b}} \tan\alpha + 2h_{\mathrm{c}} \tan\beta}{b_{\mathrm{sl}} + 2h_{\mathrm{b}} \tan\alpha + 2h_{\mathrm{c}} \tan\beta} \cdot \frac{b_{\mathrm{sl}} + 2h_{\mathrm{b}} \tan\alpha + 2h_{\mathrm{c}} \tan\beta + 2h_{\mathrm{s}} \tan\gamma}{l_{\mathrm{e}} + 2h_{\mathrm{b}} \tan\alpha + 2h_{\mathrm{c}} \tan\beta + 2h_{\mathrm{s}} \tan\gamma} \right)} E_{\mathrm{s}} \tag{11}$$

where the subscripts 'b', 'c' and 's' denote the ballast, capping and subgrade layers, respectively; ρ, E and h represent the density (kg/m^3), elastic modulus (N/m^2) and thickness (m), respectively; l_{e} and b_{sl} are the effective length (m) and width (m) of sleeper, respectively (l_{e}=l_{sl}–g_{t}); l_{sl} is sleeper length (m); g_{t} is the center to center distance between the rails (m); α, β and γ are the stress distribution angles (°) of ballast, capping and subgrade layers, respectively. The detailed derivation of Eqs. (6–11) is provided in Appendix II.

The stress distribution angle (i.e., inclination angle of the pyramid with vertical) can be evaluated using Burmister's theory of stress distribution in layered soil (Burmister 1958; Giroud and Han 2004):

$$\tan\alpha = \tan\alpha_0 \left[1 + 0.204 \left(\frac{E_{\mathrm{b}}}{E_{\mathrm{c}}} - 1 \right) \right]; \quad \tan\beta = \tan\beta_0 \left[1 + 0.204 \left(\frac{E_{\mathrm{c}}}{E_{\mathrm{s}}} - 1 \right) \right] \tag{12}$$

where α_0 and β_0 are the reference stress distribution angles in uniform ballast (i.e., for $E_{\mathrm{b}} = E_{\mathrm{c}}$) and capping (i.e., for $E_{\mathrm{c}} = E_{\mathrm{s}}$), respectively. The value of α_0 is 45° (Zhang et al. 2016). The

value of β_0 is considered as 27° based on the assumed stress distribution of 2:1 (Han et al. 2013).

It is interesting to note that the load distribution pyramids below adjacent sleepers might overlap in the longitudinal direction in case of large thickness, small sleeper spacing and high stress distribution angle (Zhai et al. 2004). Figs. 3(a), 3(b) and 3(c) show the overlapping in the pyramids along the longitudinal direction in the ballast, capping and subgrade layers, respectively. The height of the overlapped regions can be evaluated as:

$$h_{\mathrm{bl}} = h_{\mathrm{b}} - \left(\frac{S - b_{\mathrm{sl}}}{2\tan\alpha}\right) \tag{13}$$

$$h_{\mathrm{cl}} = h_{\mathrm{c}} - \left(\frac{S - b_{\mathrm{sl}} - 2h_{\mathrm{b}}\tan\alpha}{2\tan\beta}\right) \tag{14}$$

$$h_{\mathrm{sl}} = h_{\mathrm{s}} - \left(\frac{S - b_{\mathrm{sl}} - 2h_{\mathrm{b}}\tan\alpha - 2h_{\mathrm{c}}\tan\beta}{2\tan\gamma}\right) \tag{15}$$

where h_{bl}, h_{cl} and h_{sl} are the overlap height (m) in ballast, capping and subgrade along the longitudinal direction, respectively. The established pyramidal load distribution model only considers the overlapping along the longitudinal direction (Zhai et al. 2004). However, the load distribution pyramids may also overlap along the transverse direction (perpendicular to the direction of train movement) if the layer thickness and stress-distribution angles are high, and the sleeper length is small. Figs. 3(d), 3(e) and 3(f) show the overlapping along the transverse directions in ballast, capping and subgrade, respectively. The overlap height in the ballast, capping and subgrade along the transverse direction can be determined as:

$$h_{\mathrm{bt}} = h_{\mathrm{b}} - \left(\frac{l_{\mathrm{sl}} - 2l_{\mathrm{e}}}{2\tan\alpha}\right) \tag{16}$$

$$h_{\mathrm{ct}} = h_{\mathrm{c}} - \left(\frac{l_{\mathrm{sl}} - 2l_{\mathrm{e}} - 2h_{\mathrm{b}}\tan\alpha}{2\tan\beta}\right) \tag{17}$$

$$h_{\mathrm{st}} = h_{\mathrm{s}} - \left(\frac{l_{\mathrm{sl}} - 2l_{\mathrm{e}} - 2h_{\mathrm{b}}\tan\alpha - 2h_{\mathrm{c}}\tan\beta}{2\tan\gamma}\right) \tag{18}$$

where h_{bt}, h_{ct} and h_{st} are the overlap height (m) in ballast, capping and subgrade along the transverse direction, respectively. Fig. 4 shows the effective portion of the substructure layers below each sleeper point considered in the analysis. The geometry of this effective portion (consequently, the vibrating mass and stiffness of substructure layers) varies depending on the overlapping within the substructure layers. It is apparent from Fig. 4 that the stiffness and vibrating mass of the substructure layers may be over-predicted if the overlapping along the transverse direction is neglected in the analysis. Therefore, the mass and stiffness of the substructure layers can be determined more accurately if the overlapping is also considered along the transverse direction.

In summary, the overlap height is first calculated using Eqs. 13–18 and the resulting geometry of the load distribution pyramid is identified. Subsequently, the vibrating mass and stiffness of the substructure layers (effective region) is determined using a similar procedure as described in APPENDIX II. Thus, the effect of overlapping is accounted for in the analysis by modifying the vibrating mass and stiffness of the substructure layers. Nevertheless, a detailed description of the different cases (or geometries) that may arise due to overlapping, and the corresponding equations to evaluate the mass and stiffness of the substructure layers for each case will be provided by the authors upon request.

The equivalent damping coefficient of the substructure layers can be calculated as (Nimbalkar et al. 2012):

$$c_s = \sqrt{\frac{E_s \rho_s}{(1+\nu_s)(1-\nu_s)}};\ c_c = \sqrt{\frac{E_c \rho_c}{(1+\nu_c)(1-\nu_c)}};\ c_b = \sqrt{\frac{E_b \rho_b}{(1+\nu_b)(1-\nu_b)}} \tag{19}$$

where v_s, v_c and v_b are the Poisson's ratios of subgrade, capping and ballast layers, respectively. The external force $f_{b,n}(t)$ in Eq. (5) is equal to the load-time history calculated using the loading model, while the external forces $f_{s,n}(t)$ and $f_{c,n}(t)$ are considered as zero. The input parameters to evaluate the load-time history include E_r, I, S, Q and k. The parameters E_r, I and S are usually

pre-defined. The wheel load is one half of the axle load (Q_a). To account for the dynamic effects due to the wheel-rail irregularities, the wheel load can also be multiplied by the dynamic amplification factor (DAF). In the present study, DAF is evaluated using the method developed by Nimbalkar and Indraratna (2016):

$$DAF = 1 + i_1 \left(\frac{V}{D_w}\right)^{i_2} \tag{20}$$

where V is the train speed (in km/h); D_w is the wheel diameter (in m); i_1 and i_2 are the empirical parameters that depend on the axle load and subgrade type. This method was derived from the field investigations, and it accounts for the variation in load amplification due to a change in subgrade type, axle load and train speed. The value of parameters i_1 and i_2 may range between 0.0052 to 0.0065 and 0.75 to 1.02, respectively, depending on the subgrade type and axle load (Nimbalkar and Indraratna 2016).

The track modulus is calculated by modifying the approach described in Doyle (1980):

$$\frac{1}{k} = S\left(\frac{1}{k_p} + \frac{1}{k_b} + \frac{1}{k_c} + \frac{1}{k_s}\right) \tag{21}$$

where k_p is the spring constant of rail pad (N/m) (including sleeper).

Track settlement model

The cumulative settlement (or irrecoverable deformation) in the substructure layers has been predicted using the empirical models.

Settlement in granular (ballast and capping) layers

The irrecoverable deformation in ballast and capping has been calculated using a power model (Punetha et al. 2019):

$$\varepsilon_b^p = k_1^b \left(\frac{\sigma_{oct}}{P_{atm}}\right)^{k_2^b} \left(\frac{\tau_{oct}}{P_{atm}}\right)^{k_3^b} N^{k_4^b} \tag{22}$$

$$\varepsilon_{\mathrm{c}}^{p} = k_1^c \left(\frac{\sigma_{\mathrm{oct}}}{P_{\mathrm{atm}}}\right)^{k_2^c} \left(\frac{\tau_{\mathrm{oct}}}{P_{\mathrm{atm}}}\right)^{k_3^c} N^{k_4^c} \quad (23)$$

where the superscripts 'b' and 'c' denote the ballast and capping layer, respectively; k_1, k_2, k_3 and k_4 are the empirical parameters; $\varepsilon_{\mathrm{b}}{}^{p}$ and $\varepsilon_{\mathrm{c}}{}^{p}$ are the irrecoverable strains (%) in vertical direction in ballast and capping, respectively; σ_{oct} and τ_{oct} are the octahedral normal and shear stresses (N/m^2), respectively; P_{atm} is the atmospheric pressure (N/m^2); N is the number of load cycles. The parameters k_1, k_2 and k_3 represent the influence of the infill type, octahedral normal and shear stresses on the magnitude of $\varepsilon_{\mathrm{b}}{}^{p}$ (or $\varepsilon_{\mathrm{c}}{}^{p}$) corresponding to the first load cycle. The parameter k_4 governs the variation of $\varepsilon_{\mathrm{b}}{}^{p}$ (or $\varepsilon_{\mathrm{c}}{}^{p}$) with the number of load cycles. The parameters k_1, k_2, k_3 and k_4 can be evaluated by fitting the experimental curves of $\varepsilon_{\mathrm{b}}{}^{p}$ or $\varepsilon_{\mathrm{c}}{}^{p}$ with N at different loading conditions. The total settlement can be evaluated by multiplying the strain with the thickness of the ballast and capping layers.

Settlement in subgrade layers

The model developed by Li and Selig (1996) has been used to predict the irrecoverable deformation in the subgrade layer:

$$\varepsilon_{\mathrm{s}}^{p} = a \left(\frac{\sigma_{\mathrm{d}}'}{\sigma_{\mathrm{s}}}\right)^{m} N^{b} \quad (24)$$

where $\varepsilon_{\mathrm{s}}{}^{p}$ is the cumulative plastic strain in subgrade (%); σ'_{d} is the deviator stress (N/m^2); σ_{s} is the compressive strength of subgrade soil (N/m^2); a, m and b are the parameters that depend on the subgrade soil type. Table 1 shows the values of these parameters for different subgrade soil type. The subgrade is assumed to be divided into 10 layers and the strain in each layer is evaluated using Eq. (24). Subsequently, the total irrecoverable deformation (s_{s}) is calculated as:

$$s_s = \sum_{i=1}^{10} (\varepsilon_s^p)_i \, h_i \tag{25}$$

where h_i is the thickness of i^{th} subgrade layer (m); $(\varepsilon_s^{\,p})_i$ is the cumulative plastic strain in the i^{th} subgrade layer. The irrecoverable deformation is calculated after the completion of an individual load cycle. This cumulative approach is better than the calculation of irrecoverable deformation during an individual cycle, as the later approach would incur a huge amount of computational time (Suiker and De Borst 2003). The stresses in the substructure layers are calculated using the method described in Appendix I.

MODEL VALIDATION

The present method can be used to predict the resilient as well as the irrecoverable response of the ballasted railway tracks under train induced repeated loading. The response includes the resilient displacement, velocity and acceleration, and irrecoverable displacement of the substructure layers. The substructure layer response predicted using the present method is compared with the field investigation data reported by Takemiya and Bian (2005), Gräbe et al. (2005), Gräbe and Shaw (2010), Priest et al. (2010) and Mishra et al. (2014).

Takemiya and Bian (2005) reported the ground displacement and acceleration recorded during the passage of the Swedish X-2000 train at a speed of 70 km/h and 200 km/h. The track was located over very soft ground at the West Coast line in Sweden. Table 2 shows the values of the parameters used in the analysis. The ballast layer is replaced by an equivalent top soil layer in the analysis to ensure consistency with the approach used by Takemiya and Bian (2005). The train is initially at a distance of $3\pi L/4$ from the first sleeper and is assumed to travel in the positive x-direction (i.e. from left to right). A total of 25 sleepers are considered in the analysis to ensure accurate prediction of deformations and the results are reported for the central sleeper (i.e. 13^{th} sleeper). Fig. 5 compares the vertical displacement and vertical acceleration time histories computed using the present method with the data measured from

field investigations. It can be observed that the ground displacement calculated using the present method is in good agreement with the field data at a train speed of 70 km/h. For 200 km/h, the vertical displacement in the downward direction is nearly identical to the field observation. However, a little discrepancy exists in the predictions corresponding to 200 km/h as the field data also showed vertical displacement in the upward direction, which is absent in the model predictions. The accelerations predicted using the present method show a similar trend as the field data for both 70 km/h and 200 km/h, however, the peak values are underestimated.

Gräbe et al. (2005) conducted field investigations in a heavy haul track at Bloubank site in the Broodsnyersplaas–Richards Bay Coal Export Line, South Africa. The track comprises of a 300 mm thick ballast layer overlying the formation, which constitutes of four layers of selected high-quality material (each 200 mm thick) and the in-situ material (weathered tillite). The instrumentation included Multi-depth deflectometers (MDDs), pressure plates, LVDT's, accelerometers and strain gauges. These instruments were used to monitor the layer deformation (resilient and permanent), vertical stresses in substructure layers, rail and sleeper displacement, wheel load, lateral force, sleeper reaction and acceleration in rail, sleeper and ballast. Table 2 shows the values of the parameters used in the model predictions. Table 3 compares the resilient settlement and vertical stress calculated using the present method with field data. It can be observed that the model predictions are consistent with field investigations. The present method slightly under-predicts the magnitude of vertical stress just below the ballast layer (0 mm below the foundation). Gräbe and Shaw (2010) reported the variation of irrecoverable/ permanent settlement of the substructure layers below the ballast with tonnage in million gross tonnes (MGT) at the same site. Fig. 6 compares the irrecoverable deformation calculated using the present method with that reported by Gräbe and Shaw (2010). It can be

observed that the predicted results are in good agreement with the data measured from field investigations.

Priest et al. (2010) also conducted field investigations at the Bloubank site in the Broodsnyersplaas–Richards Bay Coal Export Line, South Africa. The instrumentation included geophones to measure the velocity in substructure layers (which was used to back-calculate the displacement), and a combination of remote video monitoring and particle image velocimetry to measure the sleeper displacement. Table 2 shows the parameters used to predict the response of the substructure layers. Fig. 7(a) compares the variation of the resilient deformation with time due to the passage of 26-tonne axle load coal wagons, predicted using the present method with that recorded in the field experiments. It can be observed that the predicted response is in good agreement with the field data. Fig. 7(b) shows the variation of resilient displacement with time at different depth below the sleeper due to the passage of two adjacent bogies (4 axles). It can be observed that the predicted results are consistent with the field data. The resilient displacement decreases with depth, and the influence of the individual axles in the response diminishes with depth.

The four 200 mm thick layers of selected high-quality material were replaced by a single capping layer (800 mm thick) with equivalent elastic modulus in the analysis. Therefore, the results are only available for the top of the ballast layer (0 m), bottom of the ballast layer (0.3 m) and bottom of the capping layer (1.1 m). Fig. 7(c) compares the variation of the resilient deformation with time due to the passage of 20-tonne axle load coal wagons, predicted using the present method with the field data. It can be observed that the predicted results are in good agreement with the field observations. Fig. 7(d) shows the increase in vertical stress at 800 mm below the bottom of the sleeper predicted using the present method and that using the FE analysis by Priest et al. (2010). It can be observed that the predictions using the present method are consistent with that reported by Priest et al. (2010).

Mishra et al. (2014) conducted field investigations near several bridge approaches along the Amtrak's North East Corridor in the USA. The instrumentation included MDDs to monitor the deformation of the substructure layers and strain gauges to monitor the wheel load and sleeper reactions. Table 2 shows the parameters used for the prediction of the track response. Fig. 8 compares the resilient deformation in the ballast layer due to the passage of Acela express train predicted using the present method with the field measurements. It can be observed that the predicted trend is consistent with the field data. The small discrepancy in the peak values is likely due to a slight difference in the actual and the predicted load-time history.

Thus, the proposed method in this study can predict the stresses, resilient and irrecoverable response of the track substructure layers with adequate accuracy. The method is simple and computationally efficient. It can serve as a tool to optimize the track performance by selecting the best possible combination of geomaterials in the substructure layers. The method can capture the irrecoverable deformation of the substructure layers and hence, predict the long-term performance of the track, which can be used to design and optimize the maintenance cycles.

RESULTS AND DISCUSSION

A parametric study is conducted to investigate the influence of thickness and elastic modulus of the substructure layers on the track performance. Table 2 provides the range of the substructure parameters considered in the analysis. The nominal values of the parameters are shown in the parenthesis. The results are calculated for the passage of Thalys high-speed train at a speed of 100 km/h. In each analysis, the value of one parameter is varied at a time while the other parameters are assigned the nominal values.

Influence of layer thickness

Fig. 9(a) illustrates the influence of thickness on the average irrecoverable strain accumulated in the substructure layers when the track is subjected to tonnage of 100 MGT. The average irrecoverable strain is the ratio of vertical irrecoverable deformation in a layer to its initial thickness. It can be observed from the figure that the average irrecoverable strain in the ballast, capping and subgrade layers decreases by 22, 47 and 31%, respectively, with an increase in ballast thickness (h_b) from 0.15 to 0.6 m. It is interesting to note that a 31% reduction in the subgrade strain, in this case, represents a decrease in the permanent subgrade settlement by 10 mm. This decrease in strain results from a combination of two counteracting effects. First, an increase in granular layer thickness increases the track modulus (and consequently, the rail seat load), which increases the stresses in substructure layers (Li et al. 2016). Second, an increase in h_b enhances the stress spreading ability of ballast and increases the depth of substructure layers from sleeper bottom, which decreases the stress (Li and Selig 1998). It is apparent that the second effect is dominant in this case, as there is an overall reduction in strain.

The average irrecoverable strain in capping and subgrade decreases by 76 and 29%, respectively, with an increase in capping thickness (h_c) from 0.15 to 0.45 m. However, the ballast strain increases by 1.6% with an increase in h_c. This increment is due to a rise in ballast stress with an increase in h_c for a fixed value of h_b. The increase in stress is reasonable since the second effect mentioned above is negligible for this case. The subgrade thickness (h_s) also influences the strain in the substructure layers. The average irrecoverable strain in ballast, capping and subgrade decreases by 19, 27 and 87%, respectively, with an increase in h_s from 1 to 10 m. This strain reduction in ballast and capping is due to a decrease in the stresses in the granular layers with an increase in h_s. Since, the track modulus decreases with an increase in h_s (Li et al. 2016), the rail seat load decreases and consequently, the stresses in the track layers

reduce. The average subgrade strain also decreases with an increase in h_s. This is reasonable since the contribution of the deep subgrade layers to the total subgrade settlement is minimal. Thus, it is apparent that the thickness of the substructure layers significantly influences the irrecoverable deformation response of the track substructure.

Influence of elastic modulus

Fig. 9(b) shows the variation of average irrecoverable strain accumulated in the substructure layers with the elastic modulus when the track is subjected to tonnage of 100 MGT. It can be observed that the average irrecoverable strain in ballast, capping and subgrade decreases by 9.3, 2.3 and 9%, respectively, with an increase in ballast modulus (E_b) from 138 to 551 MPa. The increase in E_b leads to an increment in the track modulus, which increases the rail seat load (Selig and Waters 1994). Consequently, the stress in the substructure layers must increase with an increase in E_b. However, a stiff ballast layer (with large E_b) distributes the load to a wider area of capping as compared to less stiff ballast layer. Therefore, the actual magnitude of the stress depends on the degree of increment of both rail seat load and the load distribution zone/area. In this case, the strain decreases, which implies that the increment in load distribution area dominates the response.

The average irrecoverable strain in capping and subgrade decreases by 30 and 3.5% with an increase in capping modulus (E_c) from 69 to 276 MPa. However, the ballast strain increases by 9.8% with an increase in E_c. The increase in ballast strain may be ascribed to a reduction in the load spread area with an increase in E_c. Burmister (1958) showed that the vertical stress at the interface of a two-layer medium increases with a reduction in the ratio of modulus of upper to lower layer materials. In the present study, this increase in vertical stress (due to a reduction in E_b/E_c ratio) is manifested by a corresponding decrease in α. Consequently, the stress and the associated strain in the ballast layer increases with an increase

403 in E_c. Nevertheless, β increases with an increase in E_c and therefore, the stress and the
404 associated strain in the capping and subgrade layers decreases.

405 It is apparent from Fig. 9(b) that E_s plays a significant role in the irrecoverable response
406 of the substructure. The average irrecoverable strain in the ballast and capping layers increases
407 by 51 and 104% with an increase in E_s from 14 to 276 MPa, respectively. However, the
408 subgrade strain decreases by 99% with an increase in E_s. An increment in E_s increases the track
409 modulus and the rail seat load (Li et al. 2016). Thus, the stresses in the substructure layers
410 increase with an increase in E_s. Consequently, the ballast and capping strain increases.
411 However, in the subgrade, the increase in stress is compensated by a corresponding increase in
412 the strength with an increment in E_s (Li et al. 2016). Therefore, the subgrade settlement
413 decreases with an increase in E_s.

414 Thus, the present method can accurately predict the variation in the irrecoverable
415 deformation of the track layers in response to the track parameters. This method may help the
416 practicing engineers to evaluate the magnitude of track substructure settlement after the
417 completion of a fixed number of load cycles (or tonnage). This may aid in the adequate
418 planning of the maintenance cycles by predicting the time when the substructure settlement
419 exceeds a permissible/safe limit. Moreover, using the present approach, the track performance
420 can be enhanced by optimizing the substructure layer parameters.

421 ASSUMPTIONS, LIMITATIONS AND FUTURE SCOPE

422 The main assumptions in the proposed method are:

423 - The distribution of vertical load from the sleeper to the substructure layers is pyramidal
424 - No-slip condition exists for the ballast-capping and capping-subgrade interfaces
425 - The track structure is symmetric with respect to the track centerline
426 - The substructure layer overlays the bedrock

The limitations of the present approach are as follows:

- Principal stress rotation: The present approach neglects the influence of principal stress rotation on the track response. The rotation of principal stress can affect the irrecoverable deformations of the geomaterials (Gräbe and Clayton 2009).
- Vehicle-track interaction: In the present study, a dynamic amplification factor has been employed to account for the additional loads applied on the track due to vehicle-track interaction, which is a simplified approach.
- Loading direction: The present approach considers loading only along the vertical direction. However, in reality, the track is subjected to a combination of loads along the vertical, lateral and longitudinal directions (Esveld 2001).

The future investigations shall address these limitations to improve the accuracy of the present approach.

CONCLUSIONS

This article presents an integrated approach to evaluate the recoverable and irrecoverable responses of the substructure layers in ballasted railway tracks. The track substructure layers have been represented as lumped masses connected by springs and dashpots, which accounts for the discrete sleeper support. The key features of the present approach include:

- consideration of more appropriate inclusion of three substructure layers (ballast, capping and subgrade), compared to the existing models simplifying track substructure as single or dual layers.
- incorporation of overlapping of the load distribution pyramids along both transverse and longitudinal directions, which is an improvement over the existing models.
- prediction of irrecoverable deformation in ballast, capping and subgrade layers using empirical settlement models for individual layers.

A good agreement between the responses predicted using the present method and the field investigations reported in the literature clearly indicates that the model can accurately predict the behavior of track substructure layers. The parametric investigation reveals that the irrecoverable deformation in the substructure layers is sensitive to the elastic modulus and thickness of individual layers. The response of each track layer is affected by the adjacent layers and the incorporation of multi-layered track structure enables more accurate prediction of track behavior. The proposed method is simple, computationally efficient and can be used readily as a tool by practicing engineers to optimize the track performance.

Appendix I. Stress calculations

The vertical stress in the ballast, capping and subgrade at any depth can be calculated using Eqs. (26), (27) and (28), respectively.

$$\sigma'_{z,b}(t) = \frac{f_{b,n}(t)}{A_b(z)} \tag{26}$$

$$\sigma'_{z,c}(t) = \frac{c_b\left[\dot{y}_{b,n}(t) - \dot{y}_{c,n}(t)\right] + k_b\left[y_{b,n}(t) - y_{c,n}(t)\right]}{A_c(z)} \tag{27}$$

$$\sigma'_{z,s}(t) = \frac{c_c\left[\dot{y}_{c,n}(t) - \dot{y}_{s,n}(t)\right] + k_c\left[y_{c,n}(t) - y_{s,n}(t)\right]}{A_s(z)} \tag{28}$$

where $\sigma'_{z,b}(t)$, $\sigma'_{z,c}(t)$ and $\sigma'_{z,s}(t)$ are the vertical stresses (N/m^2) in the ballast, capping and subgrade layers, respectively at depth z and time t; A_b (z), A_c (z) and A_s (z) are the equivalent area (m^2) of ballast, capping and subgrade layers at depth z, respectively (refer to Fig. 4). The lateral stresses (σ'_x, σ'_y) for each layer are calculated by multiplying the vertical stress with the coefficient of lateral earth pressure [k_0, (k_0=1–sin φ'; where φ' = friction angle)]. The average shear stress acting at each substructure layer can be evaluated as:

$$\boldsymbol{T}_{\boldsymbol{n}}^{\boldsymbol{s}} = 0.5\begin{bmatrix} \frac{k_{\mathrm{s}}^{s}}{A_{\mathrm{s}}^{s}} & 0 & 0 \\ 0 & \frac{k_{\mathrm{c}}^{s}}{A_{\mathrm{c}}^{s}} & 0 \\ 0 & 0 & \frac{k_{\mathrm{b}}^{s}}{A_{\mathrm{b}}^{s}} \end{bmatrix} \begin{Bmatrix} y_{\mathrm{s,n-1}}(t) + y_{\mathrm{s,n+1}}(t) - 2y_{\mathrm{s,n}}(t) \\ y_{\mathrm{c,n-1}}(t) + y_{\mathrm{c,n+1}}(t) - 2y_{\mathrm{c,n}}(t) \\ y_{\mathrm{b,n-1}}(t) + y_{\mathrm{b,n+1}}(t) - 2y_{\mathrm{b,n}}(t) \end{Bmatrix}$$
$$+ 0.5\begin{bmatrix} \frac{c_{\mathrm{s}}^{s}}{A_{\mathrm{s}}^{s}} & 0 & 0 \\ 0 & \frac{c_{\mathrm{c}}^{s}}{A_{\mathrm{c}}^{s}} & 0 \\ 0 & 0 & \frac{c_{\mathrm{b}}^{s}}{A_{\mathrm{b}}^{s}} \end{bmatrix} \begin{Bmatrix} \dot{y}_{\mathrm{s,n-1}}(t) + \dot{y}_{\mathrm{s,n+1}}(t) - 2\dot{y}_{\mathrm{s,n}}(t) \\ \dot{y}_{\mathrm{c,n-1}}(t) + \dot{y}_{\mathrm{c,n+1}}(t) - 2\dot{y}_{\mathrm{c,n}}(t) \\ \dot{y}_{\mathrm{b,n-1}}(t) + \dot{y}_{\mathrm{b,n+1}}(t) - 2\dot{y}_{\mathrm{b,n}}(t) \end{Bmatrix} \quad (29)$$

where $\boldsymbol{T}_{\mathbf{n}}^{\mathbf{s}}$ is the average shear stress vector at n^{th} sleeper point in *yz* plane; A^{s}_{b}, A^{s}_{c} and A^{s}_{s} are the equivalent shear area (m^2) of ballast, capping and subgrade layers, respectively. The shear stress is assumed to be uniformly distributed along the entire thickness of the individual substructure layers. Fig. 4 shows the equivalent normal and shear area of the substructure layers considered in the present method. The equations to evaluate the octahedral normal and shear stresses, and deviator stress can be found in Timoshenko and Goodier (1970).

Appendix II. Calculation of mass and stiffness of substructure layers

The mass of the effective region of the substructure layers is calculated by multiplying the density of each layer with its volume. Figs. 10(a), (b) and (c) show the effective portion of ballast, capping and subgrade layers, respectively, in the case of no overlapping. Consider a small element *dz* at a depth *z* from the top of the ballast layer. The area of the element [A_{b} (z)] is given by:

$$A_{\mathrm{b}}(z) = (b_{\mathrm{sl}} + 2z\tan\alpha)(l_{\mathrm{e}} + 2z\tan\alpha) \quad (30)$$

The mass of this element is calculated as:

$$dm_{\mathrm{b}} = \rho_{\mathrm{b}}(b_{\mathrm{sl}} + 2z\tan\alpha)(l_{\mathrm{e}} + 2z\tan\alpha)dz \quad (31)$$

The mass of the total effective region of ballast can then be calculated by integrating Eq. (31):

$$m_{\mathrm{b}} = \rho_{\mathrm{b}} \int_{z=0}^{z=h_{\mathrm{b}}} (b_{\mathrm{sl}} + 2z\tan\alpha)(l_{\mathrm{e}} + 2z\tan\alpha)dz \quad (32)$$

Similarly, the mass of capping and subgrade layers can be determined as:

$$m_{\mathrm{c}} = \rho_{\mathrm{c}} \int_{z=0}^{z=h_{\mathrm{c}}} (b_{\mathrm{sl}} + 2h_{\mathrm{b}} \tan\alpha + 2z\tan\beta)(l_{\mathrm{e}} + 2h_{\mathrm{b}} \tan\alpha + 2z\tan\beta)dz \tag{33}$$

$$m_{\mathrm{s}} = \rho_{\mathrm{s}} \int_{z=0}^{z=h_{\mathrm{s}}} (b_{\mathrm{sl}} + 2h_{\mathrm{b}} \tan\alpha + 2h_{\mathrm{c}} \tan\beta + 2z\tan\gamma)(l_{\mathrm{e}} + 2h_{\mathrm{b}} \tan\alpha + 2h_{\mathrm{c}} \tan\beta + 2z\tan\gamma)dz \tag{34}$$

The stiffness of ballast, capping and subgrade layers is calculated using the analogy between effective region of substructure layers and an axially loaded bar with variable cross sectional area as:

$$k_{\mathrm{b}} = \frac{E_{\mathrm{b}}}{\int \frac{dz}{A_{\mathrm{b}}(z)}} = E_{\mathrm{b}} \left[\int_{z=0}^{z=h_{\mathrm{b}}} \frac{dz}{(b_{\mathrm{sl}} + 2z\tan\alpha)(l_{\mathrm{e}} + 2z\tan\alpha)} \right]^{-1} \tag{35}$$

$$k_{\mathrm{c}} = E_{\mathrm{c}} \left[\int_{z=0}^{z=h_{\mathrm{c}}} \frac{dz}{(b_{\mathrm{sl}} + 2h_{\mathrm{b}} \tan\alpha + 2z\tan\beta)(l_{\mathrm{e}} + 2h_{\mathrm{b}} \tan\alpha + 2z\tan\beta)} \right]^{-1} \tag{36}$$

$$k_{\mathrm{s}} = E_{\mathrm{s}} \left[\int_{z=0}^{z=h_{\mathrm{s}}} \frac{dz}{(b_{\mathrm{sl}} + 2h_{\mathrm{b}} \tan\alpha + 2h_{\mathrm{c}} \tan\beta + 2z\tan\gamma)(l_{\mathrm{e}} + 2h_{\mathrm{b}} \tan\alpha + 2h_{\mathrm{c}} \tan\beta + 2z\tan\gamma)} \right]^{-1} \tag{37}$$

A similar procedure is employed to evaluate the mass and stiffness of the substructure layers in case of overlapping along the longitudinal and transverse directions.

DATA AVAILABILITY STATEMENT

Some or all data, models, or code that support the findings of this study are available from the corresponding author upon reasonable request.

ACKNOWLEDGMENTS

This research is financially supported by an Australian Government Research Training Program Scholarship. This support is gratefully acknowledged.

Notation

The following symbols are used in this paper:

a, m, b = empirical parameters that depend on the type of subgrade soil;
$A_b(z)$, $A_c(z)$, $A_s(z)$ = equivalent area of ballast, capping and subgrade layers at depth z, respectively (m^2);
A^s_b, A^s_c, A^s_s = equivalent shear area of ballast, capping and subgrade layers, respectively (m^2);
a_t = total number of wheels/axles under consideration;
b_{sl} = width of sleeper (m);
c_b, c_c, c_s = damping coefficients of ballast, capping and subgrade, respectively (Ns/m);
c^s_b, c^s_c, c^s_s = shear damping coefficients of ballast, capping and subgrade, respectively (Ns/m);
D_w = wheel diameter (m);
E_r, E_b, E_c, E_s = elastic modulus of rail, ballast, capping and subgrade, respectively (N/m^2);
$f_{s,n}$, $f_{c,n}$, $f_{b,n}$ = external forces acting on the subgrade, capping and ballast, respectively (N);
g_t = centre-to-centre distance between the rails (m);
h_b, h_c, h_s = thickness of ballast, capping and subgrade, respectively (m);
h_{bl}, h_{bt} = overlap height in ballast along longitudinal and transverse direction, respectively (m);
h_{cl}, h_{ct} = overlap height in capping along longitudinal and transverse direction, respectively (m);
h_i = thickness of i^{th} subgrade layer (m);
h_{sl}, h_{st} = overlap height in subgrade along longitudinal and transverse direction, respectively (m);
I = moment of inertia of rail (m^4);
i_1, i_2 = empirical parameters that depend on the axle load and subgrade type;
k = track modulus (N/m^2);
k_0 = coefficient of lateral earth pressure;
k_1^b, k_2^b, k_3^b, k_4^b = empirical parameters for ballast;
k_1^c, k_2^c, k_3^c, k_4^c = empirical parameters for capping;
k_b, k_c, k_s = stiffness of ballast, capping and subgrade, respectively (N/m);
k_p = spring constant of rail pad (including sleeper) (N/m);
k^s_b, k^s_c k^s_s = shear stiffness of ballast, capping and subgrade, respectively (N/m);
L = characteristic length (m);
l_e = effective length of sleeper (m);
l_{sl} = length of sleeper (m);
m_b, m_c, m_s = vibrating mass of ballast, capping and subgrade, respectively (kg);
N = number of load cycles;
P_{atm} = atmospheric pressure (N/m^2);
Q = static wheel load (N);
Q_a = static axle load (N);
$Q_{r,n}$ = rail seat load at n^{th} sleeper (N);
S = sleeper spacing (m);
s_s = total irrecoverable deformation in subgrade (m);
$\boldsymbol{T}^{\mathbf{s}}_{\mathbf{n}}$ = average shear stress vector at n^{th} sleeper point in yz plane;
V = train speed (m/s);
x_{nj} = distance between the n^{th} sleeper and j^{th} wheel/axle (m);
$\ddot{y}_{b,n}$, $\dot{y}_{b,n}$ $y_{b,n}$ = acceleration, velocity and displacement for ballast below n^{th} sleeper, respectively;
$\ddot{y}_{c,n}$, $\dot{y}_{c,n}$, $y_{c,n}$ = acceleration, velocity and displacement for capping below n^{th} sleeper, respectively;
$\ddot{y}_{s,n}$, $\dot{y}_{s,n}$ and $y_{s,n}$ = acceleration, velocity and displacement of subgrade below n^{th} sleeper, respectively;
α, β, γ = stress distribution angles for ballast, capping and subgrade, respectively (°);
α_0, β_0 = reference stress distribution angles for ballast and capping, respectively (°);

$\delta(x)$ = vertical deflection of track at distance 'x' (m);
ε_b^p, ε_c^p, ε_s^p = irrecoverable strain in ballast, capping and subgrade, respectively (%);
$(\varepsilon_s^p)_i$ = cumulative plastic strain in the i^{th} subgrade layer;
ν_b, ν_c, ν_s = Poisson's ratio of ballast, capping and subgrade, respectively;
ρ_b, ρ_c, ρ_s = density of ballast, capping and subgrade, respectively (kg/m^3);
σ'_d = deviator stress (N/m^2);
σ_{oct}, τ_{oct} = octahedral normal and shear stresses, respectively (N/m^2);
σ_s = compressive strength of the soil (N/m^2);
σ'_x, σ'_y = lateral stresses in longitudinal and transverse directions, respectively (N/m^2);
$\sigma'_{z,b}$, $\sigma'_{z,c}$, $\sigma'_{z,s}$ = vertical stresses in the ballast, capping and subgrade layers, respectively (N/m^2);
φ' = friction angle (°);

Supplemental Data (#1 vibrating mass and stiffness of substructure layers)

The equations to evaluate the mass and stiffness of the substructure layers for different cases of overlapping will be provided by the corresponding author upon request.

REFERENCES

Ahlbeck, D. R., Meacham, H. C., and Prause, R. H. (1975). "The development of analytical models for railroad track dynamics." *Symp. on Railroad Track Mechanics*, Pergamon Press, Princeton University, 239-263.

Banimahd, M., Woodward, P., Kennedy, J., and Medero, G. (2013). "Three-dimensional modelling of high speed ballasted railway tracks." *Proc. Inst. Civ. Eng. Transp.*, 166(2), 113-123.

Basu, D., and Kameswara Rao, N. S. V. (2013). "Analytical solutions for Euler-Bernoulli beam on visco-elastic foundation subjected to moving load." *Int. J. Numer. Anal. Methods Geomech.*, 37(8), 945-960.

Bian, X., Jiang, H., and Chen, Y. (2010). "Accumulative deformation in railway track induced by high-speed traffic loading of the trains." *Earthq. Eng. Eng. Vib.*, 9(3), 319-326.

Burmister, D. (1958). "Evaluation of pavement systems of the WASHO road test by layered system methods." *Highway Research Board Bulletin*, 177, 26–54.

Chen, J., and Zhou, Y. (2018). "Dynamic responses of subgrade under double-line high-speed railway." *Soil Dyn. Earthquake Eng.*, 110, 1-12.

Chen, Y. H., and Huang, Y. H. (2000). "Dynamic stiffness of infinite Timoshenko beam on viscoelastic foundation in moving co- ordinate." *Int. J. Numer. Methods Eng.*, 48(1), 1-18.

Choudhury, D., Bharti, R. K., Chauhan, S., and Indraratna, B. (2008). "Response of multilayer foundation system beneath railway track under cyclic loading." *J. Geotech. Geoenviron. Eng.*, 134(10), 1558-1563.

Connolly, D., Giannopoulos, A., and Forde, M. (2013). "Numerical modelling of ground borne vibrations from high speed rail lines on embankments." *Soil Dyn. Earthquake Eng.*, 46, 13–19.

Costa, P., Calçada, R., Cardoso, A., and Bodare, A. (2010). "Influence of soil non-linearity on the dynamic response of high-speed railway tracks." *Soil Dyn. Earthquake Eng.*, 30(4), 221–235.

Dieterman, H., and Metrikine, V. (1997). "Steady-state displacements of a beam on an elastic half-space due to a uniformly moving constant load." *Eur. J. Mech. A. Solids*, 16(2), 295-306.

Doyle, N. F. (1980). "Railway track design a review of current practice." B. o. T. Economics, ed., Australian government publishing service, Canberra.

Esveld, C. (2001). *Modern railway track*, MRT-Productions, Delft, The Netherlands.

Galvín, P., Mendoza, D., Connolly, D., Degrande, G., Lombaert, G., and Romero, A. (2018). "Scoping assessment of free-field vibrations due to railway traffic." *Soil Dyn. Earthquake Eng.*, 114, 598–614.

Galvín, P., Romero, A., and Domínguez, J. (2010). "Fully three-dimensional analysis of high-speed train–track–soil-structure dynamic interaction." *J. Sound Vib.*, 329(24), 5147-5163.

Giroud, J., and Han, J. (2004). "Design method for geogrid-reinforced unpaved roads. I. Development of design method." *J. Geotech. Geoenviron. Eng.*, 130(8), 776–786.

Gräbe, P., Clayton, C., and Shaw, F. (2005). "Deformation measurement on a heavy haul track formation." *8th International Heavy Haul Conference*, International Heavy Haul Association, Rio de Janeiro, Brazil.

Gräbe, P., and Shaw, F. (2010). "Design life prediction of a heavy haul track foundation." *Proc Inst Mech Eng F Rail Rapid Transit* 224(5), 337–344.

Gräbe, P. J., and Clayton , C. R. I. (2009). "Effects of Principal Stress Rotation on Permanent Deformation in Rail Track Foundations." *Journal of Geotechnical and Geoenvironmental Engineering*, 135(4), 555-565.

Guo, Y., and Zhai, W. (2018). "Long-term prediction of track geometry degradation in high-speed vehicle–ballastless track system due to differential subgrade settlement." *Soil Dyn. Earthquake Eng.*, 113, 1-11.

612 Hall, L. (2003). "Simulations and analyses of train-induced ground vibrations in finite element
613 models." *Soil Dyn. Earthquake Eng.*, 23(5), 403-413.
614 Han, J., Acharya, R., Parsons, R., and Khatri, D. (2013). "Improved load distribution for load
615 rating of low-fill box structures." *K-TRAN: KU12-3*, Kansas Department of
616 Transportation.
617 Hung, H., Chen, G., and Yang, Y. (2013). "Effect of railway roughness on soil vibrations due
618 to moving trains by 2.5 D finite/infinite element approach." *Eng. Struct.*, 57, 254–266.
619 Karlström, A., and Boström, A. (2006). "An analytical model for train-induced ground
620 vibrations from railways." *J. Sound Vib.*, 292(1-2), 221-241.
621 Kaynia, A. M., Madshus, C., and Zackrisson, P. (2000). "Ground vibration from high-speed
622 trains: Prediction and countermeasure." *J. Geotech. Geoenviron. Eng.*, 126(6), 531-537.
623 Kuo, C. M., and Huang, C. H. (2009). "Two approaches of finite-element modeling of ballasted
624 railway track." *J. Geotech. Geoenviron. Eng.*, 135(3), 455-458.
625 Li, D., Hyslip, J., Sussmann, T., and Chrismer, S. (2016). *Railway geotechnics*, Taylor and
626 Francis, Boca Raton, USA.
627 Li, D., and Selig, E. T. (1996). "Cumulative plastic deformation for fine-grained subgrade
628 soils." *Journal of Geotechnical Engineering* 122(12), 1006-1013.
629 Li, D., and Selig, E. T. (1998). "Method for railroad track foundation design. I: Development."
630 *Journal of Geotechnical Engineering*, 124(4), 316-322.
631 Li, L., Nimbalkar, S., and Zhong, R. (2018). "Finite element model of ballasted railway with
632 infinite boundaries considering effects of moving train loads and Rayleigh waves." *Soil*
633 *Dyn. Earthquake Eng.*, 114, 147-153.
634 Metrikine, A. V., and Popp, K. (1999). "Vibration of a periodically supported beam on an
635 elastic half-space." *Eur. J. Mech. A. Solids*, 18(4), 679-701.
636 Mishra, D., Qian, Y., Huang, H., and Tutumluer, E. (2014). "An integrated approach to
637 dynamic analysis of railroad track transitions behavior." *Transp. Geotech.*, 1(4), 188-
638 200.
639 Nguyen, K., Villalmanzo, D., Goicolea, J., and Gabaldon, F. (2016). "A computational
640 procedure for prediction of ballasted track profile degradation under railway traffic
641 loading." *Proc Inst Mech Eng F J Rail Rapid Transit*, 230(8), 1812–1827.
642 Nimbalkar, S., and Indraratna, B. (2016). "Improved performance of ballasted rail track using
643 geosynthetics and rubber shockmat." *J. Geotech. Geoenviron. Eng.*, 142(8).

644 Nimbalkar, S., Indraratna, B., Dash, S. K., and Christie, D. (2012). "Improved Performance of
645 Railway Ballast under Impact Loads Using Shock Mats." *Journal of Geotechnical and*
646 *Geoenvironmental Engineering*, 138(3), 281-294.
647 Oscarsson, J., and Dahlberg, T. (1998). "Dynamic train/track/ballast interaction - computer
648 models and full-scale experiments." *Veh. Syst. Dyn.*, 29(S1), 73-84.
649 Powrie, W., Yang, L. A., and Clayton, C. R. I. (2007). "Stress changes in the ground below
650 ballasted railway track during train passage." *Proc. Inst. Mech. Eng. F. J. Rail Rapid*
651 *Transit* 221(F2), 247-262.
652 Priest, J. A., Powrie, W., Yang, L., Grabe, P. J., and Clayton, C. R. I. (2010). "Measurements
653 of transient ground movements below a ballasted railway line." *Géotechnique*, 60(9),
654 667-677.
655 Punetha, P., Nimbalkar, S., and Khabbaz, H. (2019). "Evaluation of additional confinement for
656 three-dimensional geoinclusions under general stress state." *Can. Geotech. J.*
657 Sayeed, M. A., and Shahin, M. A. (2016). "Three-dimensional numerical modelling of
658 ballasted railway track foundations for high-speed trains with special reference to
659 critical speed." *Transp. Geotech.*, 6, 55-65.
660 Selig, E. T., and Waters, J. M. (1994). *Track geotechnology and substructure management*,
661 Thomas Telford, London.
662 Shahu, J., Kameswara Rao, N., and Yudhbir (1999). "Parametric study of resilient response of
663 tracks with a sub-ballast layer." *Can. Geotech. J.*, 36(6), 1137–1150.
664 Sheng, X., Jones, C. J. C., and Petyt, M. (1999). "Ground vibration generated by a harmonic
665 load acting on a railway track." *J. Sound Vib.*, 225(1), 3-28.
666 Stewart, H., and Selig, E. (1982). "Predicted and measured resilient response of track." *Journal*
667 *of Geotechnical Engineering Division*, 108(11), 1423–1442.
668 Suiker, A. S. J., and De Borst, R. (2003). "A numerical model for the cyclic deterioration of
669 railway tracks." *Int. J. Numer. Methods Eng.*, 57(4), 441-470.
670 Suiker, A. S. J., Selig, E. T., and Frenkel, R. (2005). "Static and cyclic triaxial testing of ballast
671 and subballast." *J. Geotech. Geoenviron. Eng.*, 131(6), 771-782.
672 Sun, Q. D., Indraratna, B., and Nimbalkar, S. (2016). "Deformation and degradation
673 mechanisms of railway ballast under high frequency cyclic loading." *J. Geotech.*
674 *Geoenviron. Eng.*, 142(1).
675 Sun, Y. Q., and Dhanasekar, M. (2002). "A dynamic model for the vertical interaction of the
676 rail track and wagon system." *Int. J. Solids Struct.*, 39(5), 1337-1359.

677 Takemiya, H., and Bian, X. (2005). "Substructure simulation of inhomogeneous track and
678 layered ground dynamic interaction under train passage." *J. Eng. Mech.*, 131(7), 699-
679 711.
680 Timoshenko, S. P., and Goodier, J. N. (1970). *Theory of elasticity*, McGraw Hill, New York.
681 Yang, L. A., Powrie, W., and Priest, J. A. (2009). "Dynamic stress analysis of a ballasted
682 railway track bed during train passage." *J. Geotech. Geoenviron. Eng.*, 135(5), 680-
683 689.
684 Yang, Y. B., and Hung, H. H. (2001). "A 2.5D finite/infinite element approach for modelling
685 visco- elastic bodies subjected to moving loads." *Int. J. Numer. Methods Eng.*, 51(11),
686 1317-1336.
687 Zhai, W., Wang, K., and Cai, C. (2009). "Fundamentals of vehicle–track coupled dynamics."
688 *Veh. Syst. Dyn.*, 47(11), 1349-1376.
689 Zhai, W. M., Wang, K. Y., and Lin, J. H. (2004). "Modelling and experiment of railway ballast
690 vibrations." *J. Sound Vib.*, 270(4-5), 673-683.
691 Zhang, T. W., Cui, Y. J., Lamas-Lopez, F., Calon, N., and Costa D'Aguiar, S. (2016).
692 "Modelling stress distribution in substructure of French conventional railway tracks."
693 *Constr. Build. Mater.*, 116, 326-334.

694

TABLES

Table 1. Parameters *a*, *b* and *m* for different subgrade soils [adapted from (Li and Selig 1996)]

Subgrade soil type	*a*	*b*	*m*
ML (silt)	0.64	0.06–0.17	1.4–2.0
MH (silt of high plasticity)	0.84	0.08–0.19	1.3–4.2
CL (clay of low plasticity)	0.30–3.5	0.08–0.34	1.0–2.6
CH (clay of high plasticity)	0.82–1.5	0.12–0.27	1.3–3.9

Table 2. Parameters used for evaluation of track response

Variable	Symbol	Unit	Takemiya and Bian (2005)	Gräbe et al. (2005); Gräbe and Shaw (2010)	Priest et al. (2010)	Mishra et al. (2014)	Present study
Ballast (Top layer)							
Elastic modulus	E_b	MPa	23	80	80	69	138–551 (276)
Poisson's ratio	ν_b	–	0.45	0.3	0.3	0.3	0.3
Shear stiffness	k_b^s	MN/m	1	0.1	0.1	78.4	78.4
Shear damping	c_b^s	kNs/m	80	80	80	80	80
Density	ρ_b	kg/m^3	1,500	1,800	1,800	1,990	1,760
Thickness	h_b	m	1	0.3	0.3	0.305	0.15–0.6 (0.3)
Capping (Middle layer)							
Elastic modulus	E_c	MPa	6	140	140	55	69–276 (138)
Poisson's ratio	ν_c	–	0.45	0.3	0.3	0.4	0.35
Shear stiffness	k_c^s	MN/m	250	476	476	1,600	476
Shear damping	c_c^s	kNs/m	800	80	80	80	80
Density	ρ_c	kg/m^3	1,260	2,300	2,300	2,092	1,920
Thickness	h_c	m	3	0.8	0.8	0.127	0.15–0.45 (0.15)
Subgrade							
Elastic modulus	E_s	MPa	44	600	600	45	14–276 (14)
Poisson's ratio	ν_s	–	0.45	0.25	0.25	0.4	0.35
Shear stiffness	k_s^s	MN/m	3,000	1,600	1,600	1,600	1,600
Shear damping	c_s^s	kNs/m	800	80	80	80	80
Density	ρ_s	kg/m^3	1,475	2,300	2,300	2,092	1,920
Thickness	h_s	m	44	3.29	3.29	2	1– 10 (4.5)

Note: The values of shear stiffness and damping have been calculated using a trial and error procedure. The initial values for the trial and error procedure, and the parametric study were chosen according to those reported by Zhai et al. (2004) and Oscarsson and Dahlberg (1998); empirical parameters for irrecoverable deformation are taken from Sun et al. (2016) and Suiker et al. (2005) for ballast and capping, respectively.

Table 3. Comparison of results reported by Gräbe et al. (2005) with model predictions

Depth below foundation (mm)	Settlement (mm)		Vertical stress (kPa)	
	Gräbe et al. (2005)	Model prediction	Gräbe et al. (2005)	Model prediction
0	0.54	0.51	110	84
400	–	–	76	75
800	0.23	0.18	59.6	53

LIST OF FIGURES

Fig. 1(a). Configuration of Thalys high-speed train; **(b).** calculation of track deflection at time t_1; **(c).** calculation of track deflection at time t_2; **(d).** final rail seat load-time history

Fig. 2. Three degree of freedom mass-spring-dashpot (MSD) model of track

Fig. 3. Overlapping along longitudinal direction in **(a).** ballast; **(b).** capping; **(c).** subgrade; transverse direction in **(d).** ballast; **(e).** capping; **(f).** subgrade

Fig. 4. Effective portion of substructure layers considered in analysis

Fig. 5. Comparison of vertical displacement and acceleration time histories predicted using the present method with field results reported by Takemiya and Bian (2005)

Fig. 6. Comparison of model predictions with the field results reported by Gräbe and Shaw (2010)

Fig. 7. Comparison of model predictions with results reported by Priest et al. (2010): **(a).** resilient displacement for 26-tonne axle load coal wagons; **(b).** resilient displacement at different depth below the sleeper; **(c).** resilient displacement for 20-tonne axle load coal wagons **(d).** vertical stress at 800 mm below sleeper bottom

Fig. 8. Comparison of model predictions with field results reported by Mishra et al. (2014)

Fig. 9. Variation of average irrecoverable strain in substructure layers with **(a).** thickness; **(b).** elastic modulus

Fig. 10. Effective region of (a) ballast; (b) capping and (c) subgrade layers

Figure 1

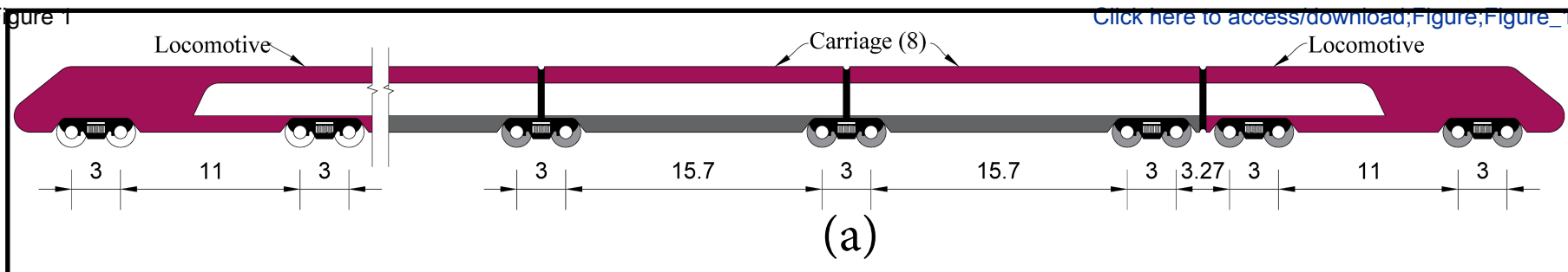

(a)

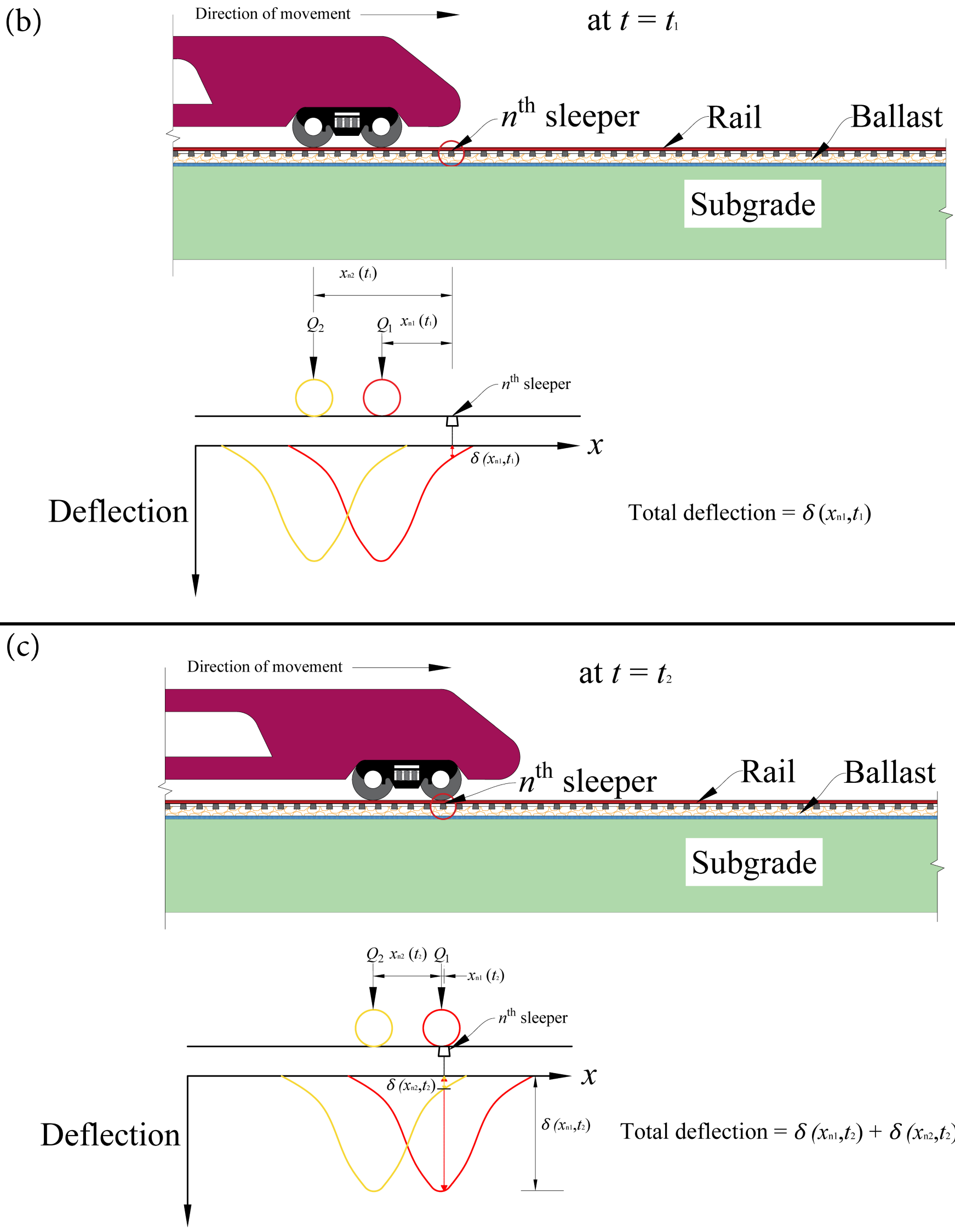

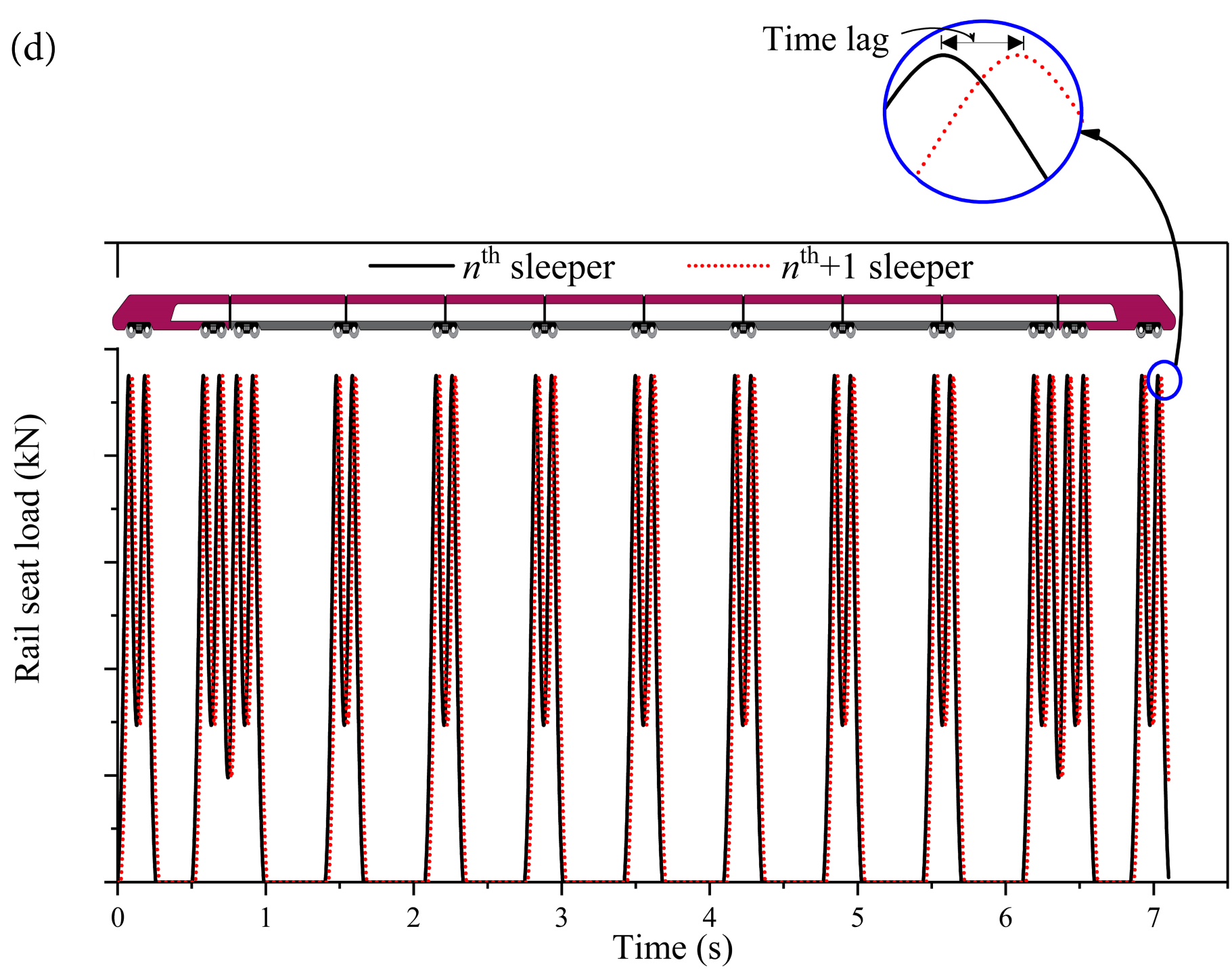

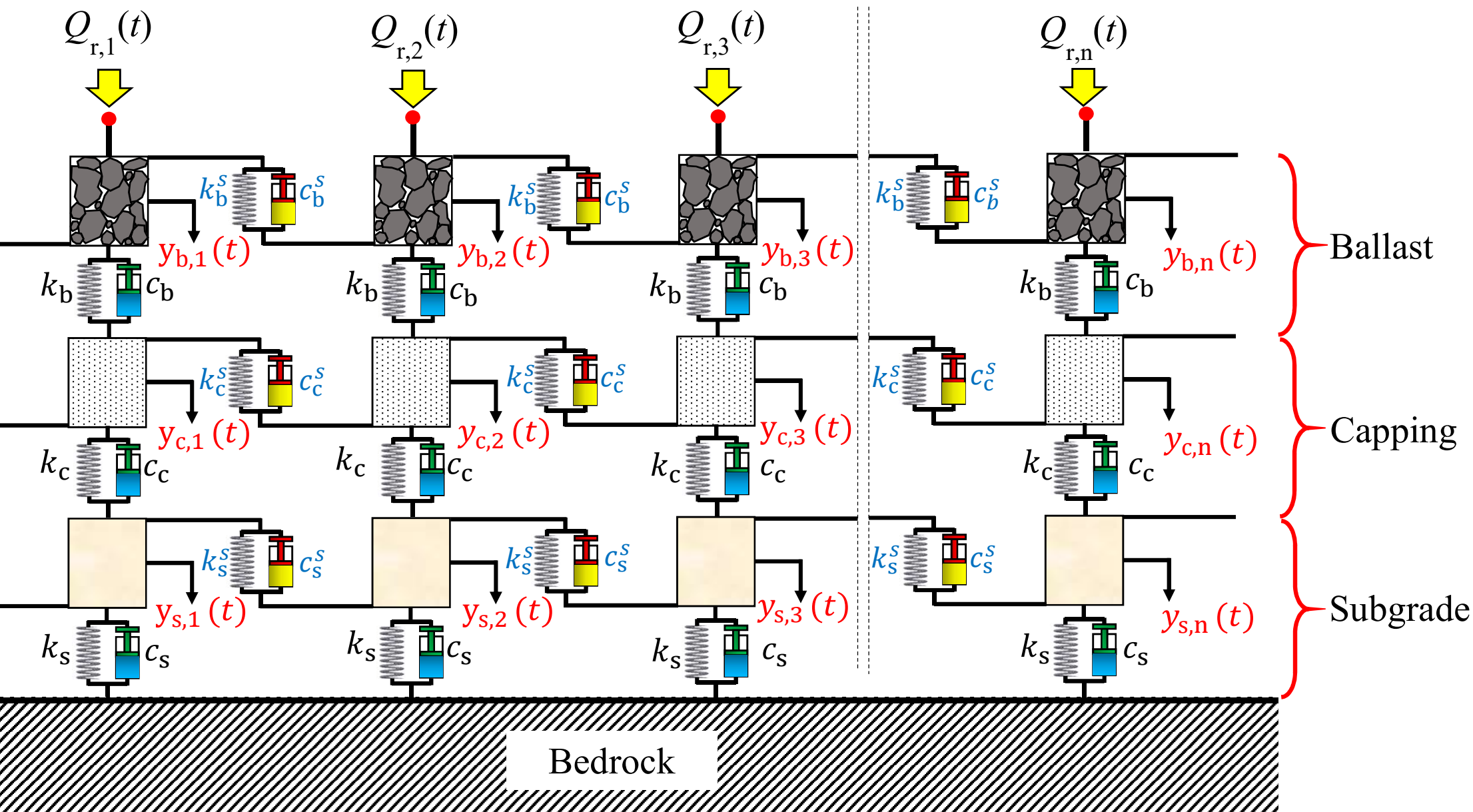
$Q_{r,1}(t)$
$Q_{r,2}(t)$
$Q_{r,3}(t)$
$Q_{r,n}(t)$
k_b^s
c_b^s
k_c^s
c_c^s
k_s^s
c_s^s
$y_{b,1}(t)$
$y_{b,2}(t)$
$y_{b,3}(t)$
$y_{b,n}(t)$
$y_{c,1}(t)$
$y_{c,2}(t)$
$y_{c,3}(t)$
$y_{c,n}(t)$
$y_{s,1}(t)$
$y_{s,2}(t)$
$y_{s,3}(t)$
$y_{s,n}(t)$
k_b
c_b
k_c
c_c
k_s
c_s
Ballast
Capping
Subgrade
Bedrock

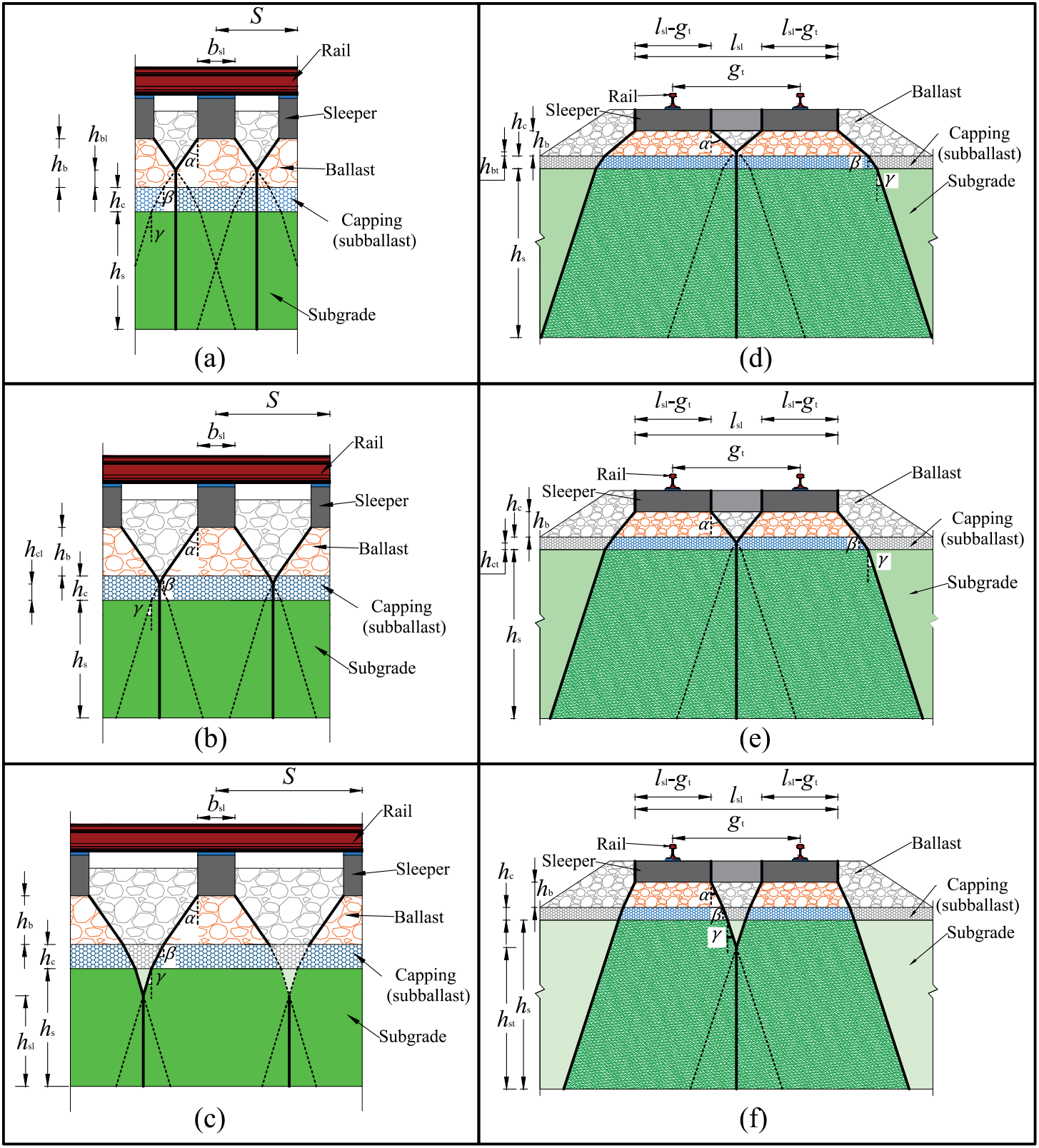
S
b_{sl}
Rail
Sleeper
Ballast
Capping
(subballast)
Subgrade
h_{bl}
h_b
h_c
h_s
α
β
γ
(a)
l_{sl}-g_t
l_{sl}
g_t
h_{bt}
(d)
h_{cl}
h_{ct}
(b)
(e)
h_{sl}
h_{st}
(c)
(f)

Figure 4

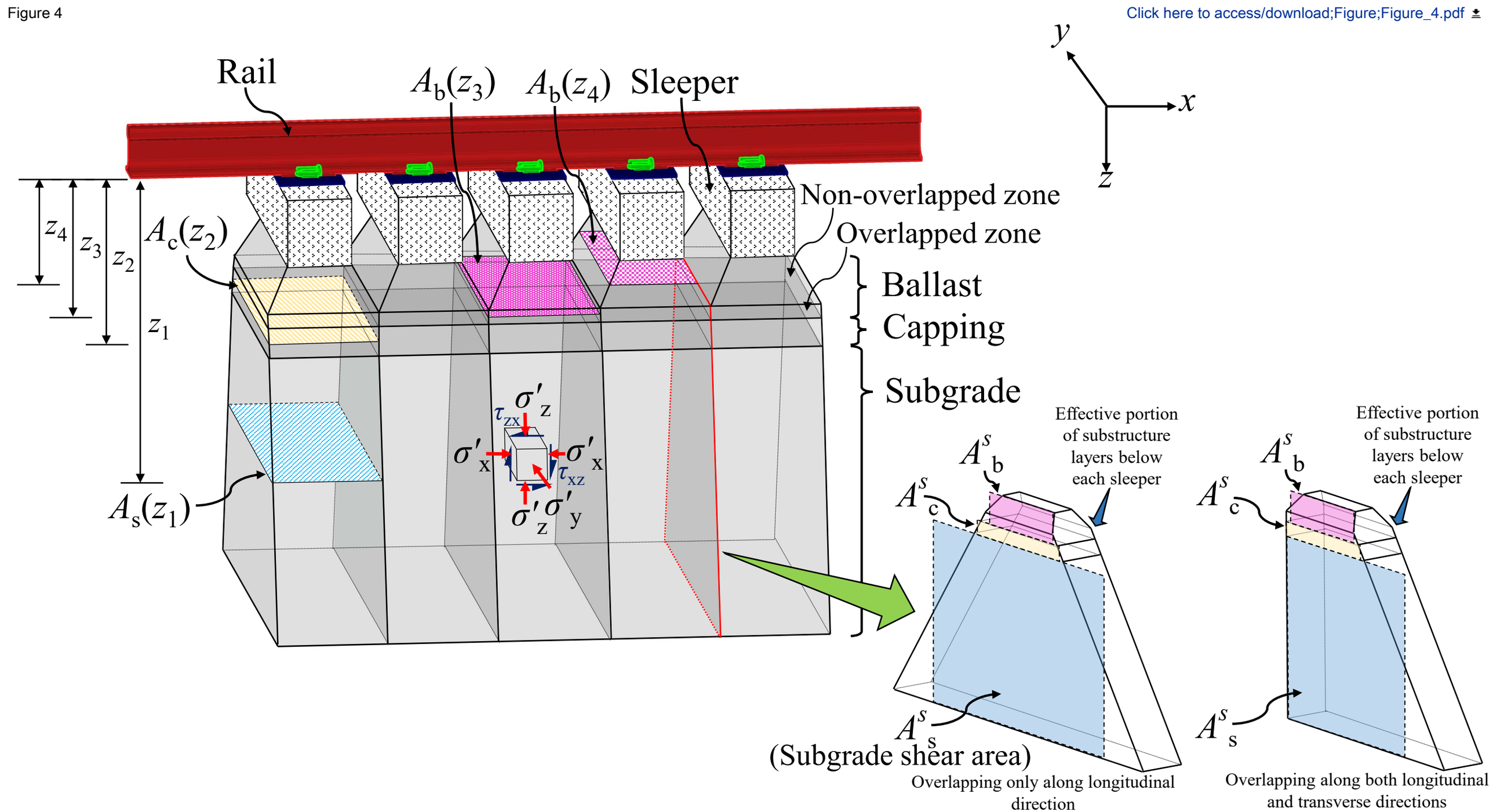

Figure 5

Click here to access/download;Figure;Figure_5.pdf

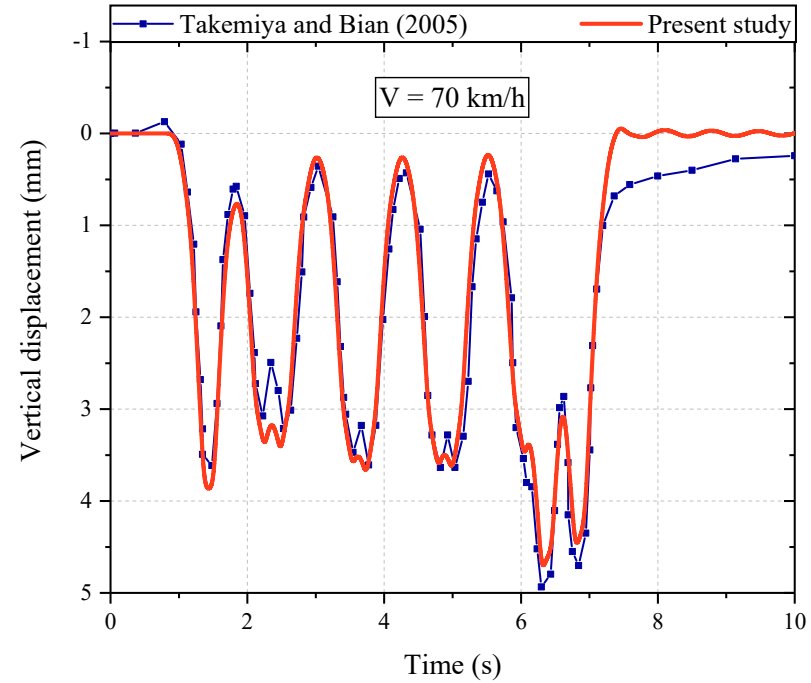

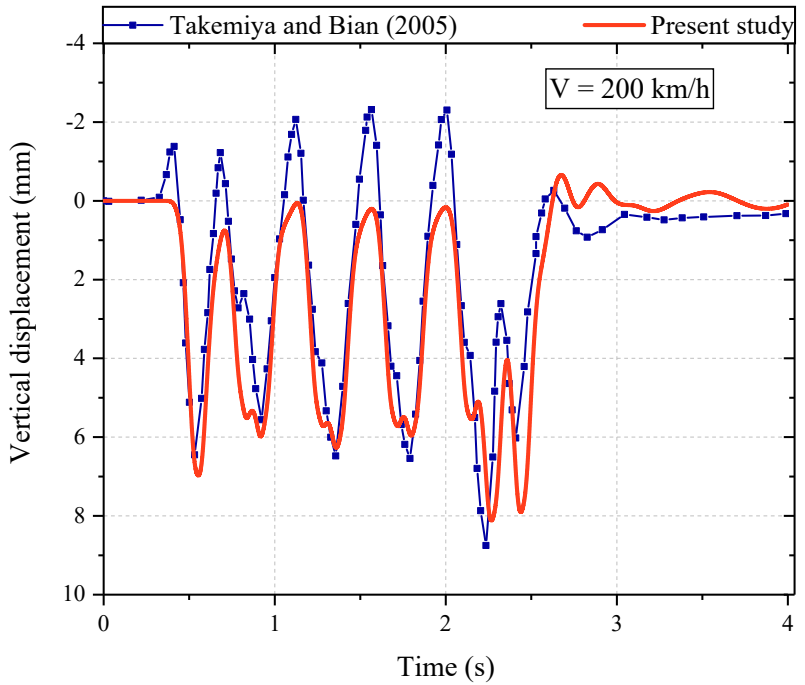

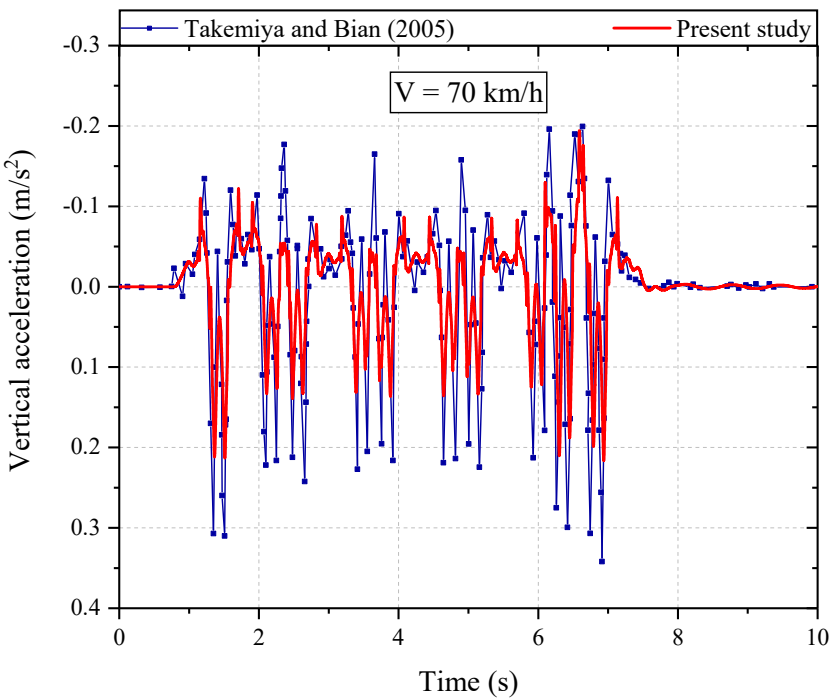

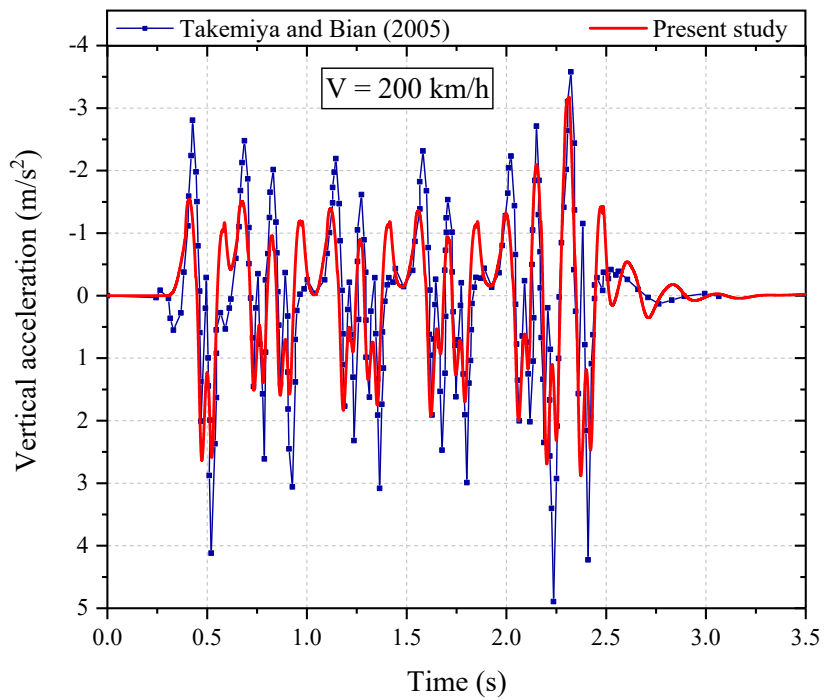

$D_w = 1.016$ m
$Q_a = 118–180$ kN
$i_1 = 0.0065$
$i_2 = 1$
$g_t = 1.6$ m
$E_r = 207$ GPa
$I = 3.04\times10^{-5}$ m^4
$b_{sl} = 0.4$ m
$l_{sl} = 3.1$ m
$S = 0.65$ m
$k_p = 54$ MN/m
$\alpha_0 = 27°$
$\beta_0 = 27°$
$\gamma = 27°$

Figure 6

Click here to access/download;Figure;Figure_6.pdf

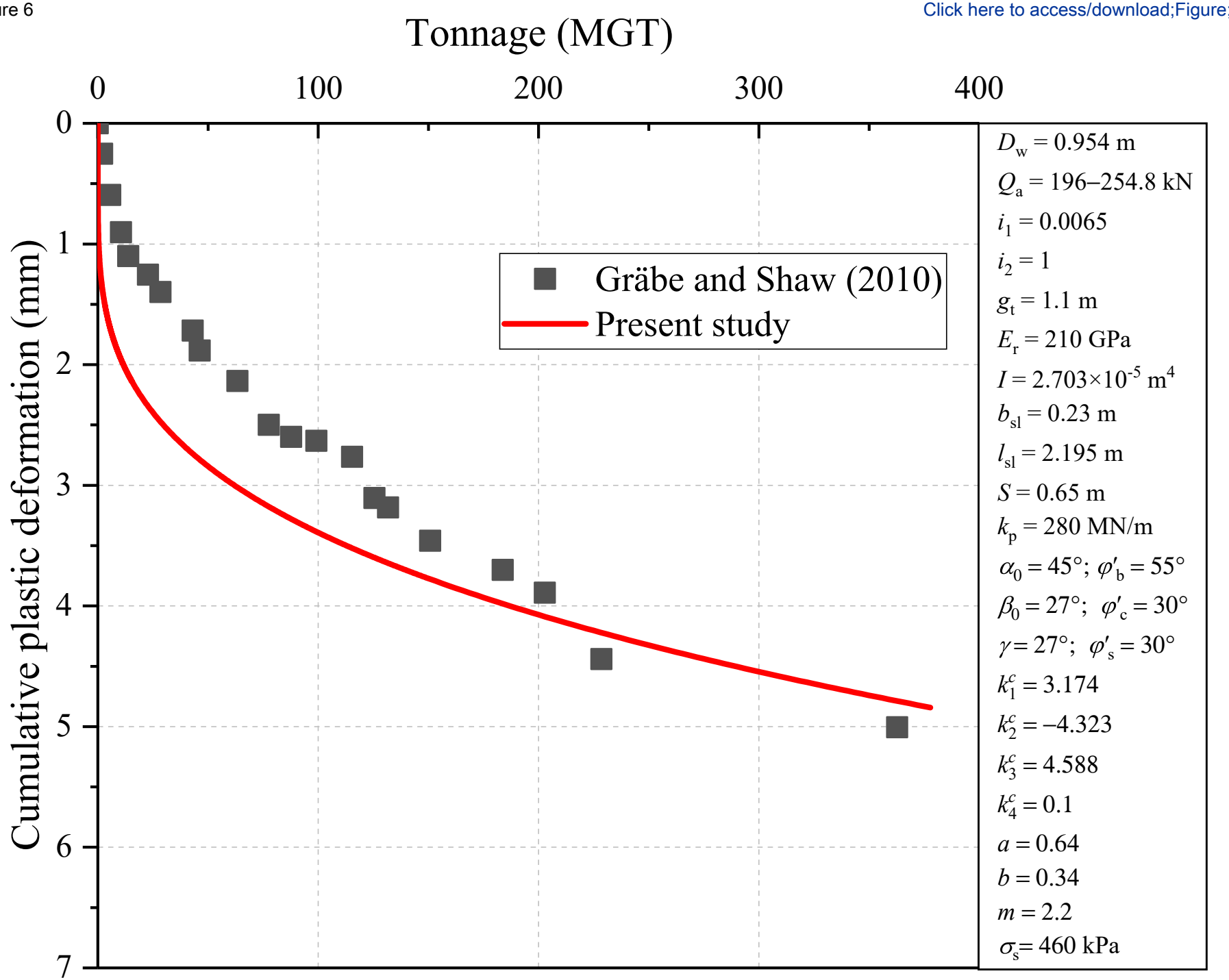

Figure 7

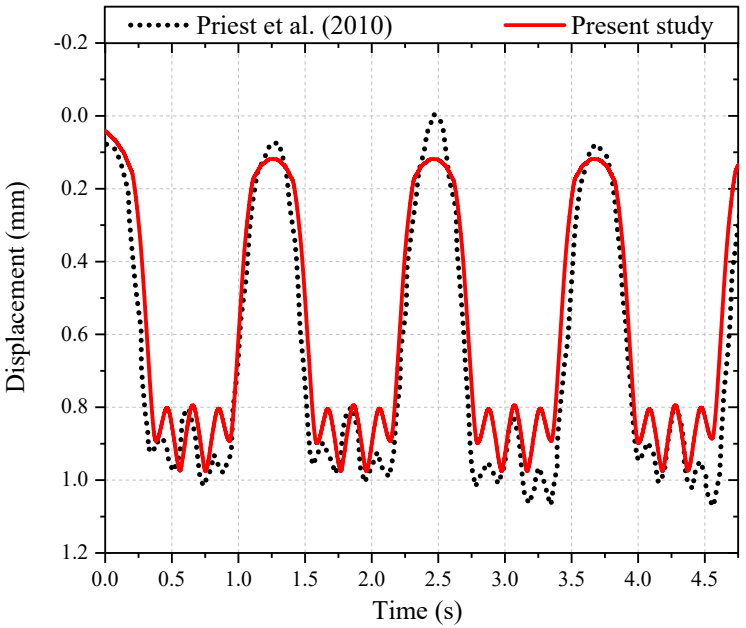

(a)

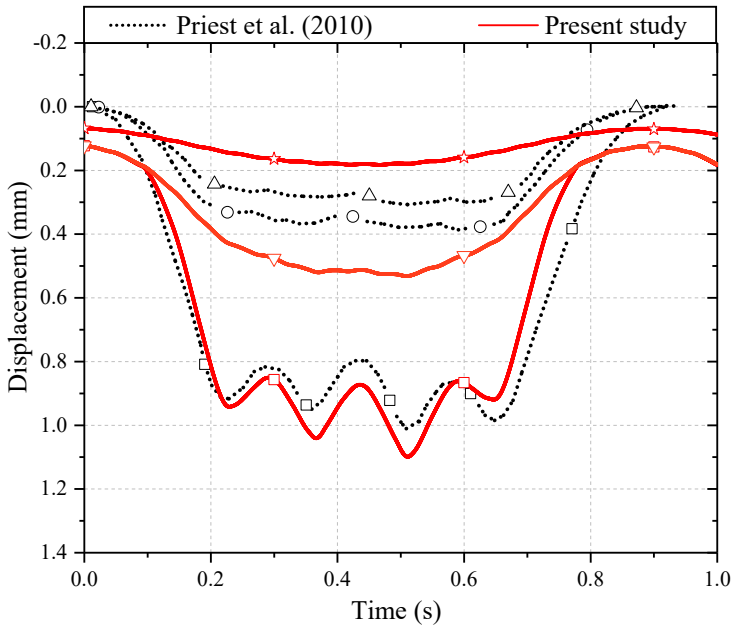

(b)

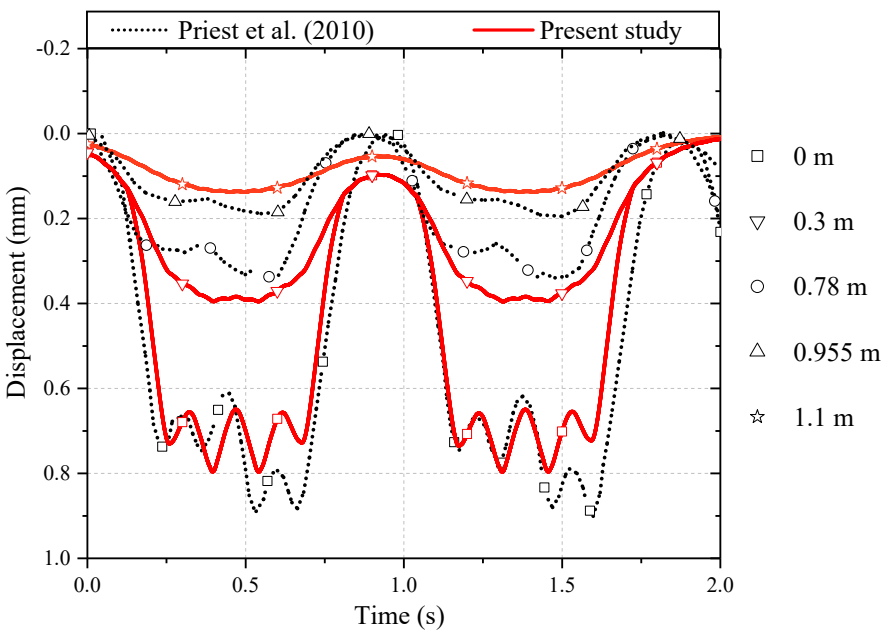

(c)

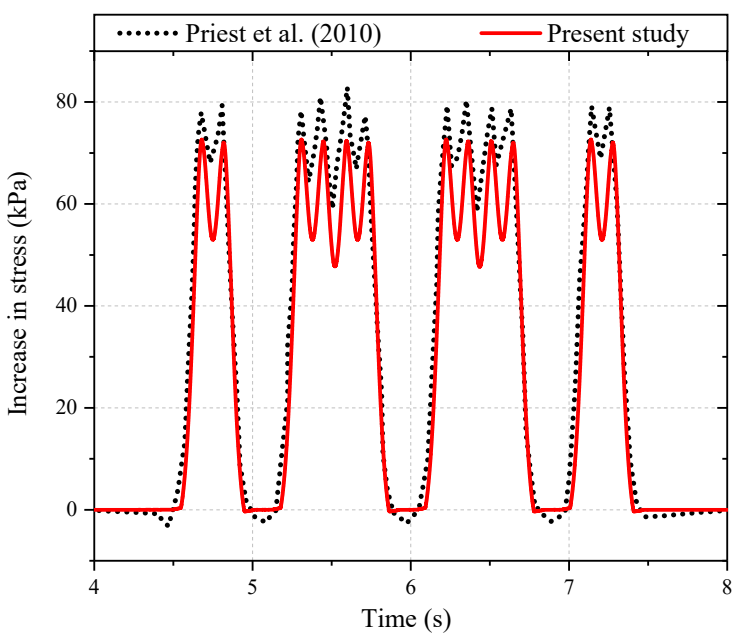

(d)

$D_w = 0.954$ m
$Q_a = 196–277$ kN
$i_1 = 0.0065$
$i_2 = 1$
$g_t = 1.1$ m
$E_r = 210$ GPa
$I = 2.703\times10^{-5}$ m^4
$b_{sl} = 0.23$ m
$l_{sl} = 2.195$ m
$S = 0.65$ m
$k_p = 280$ MN/m
$\alpha_0 = 45°$
$\beta_0 = 27°$
$\gamma = 27°$

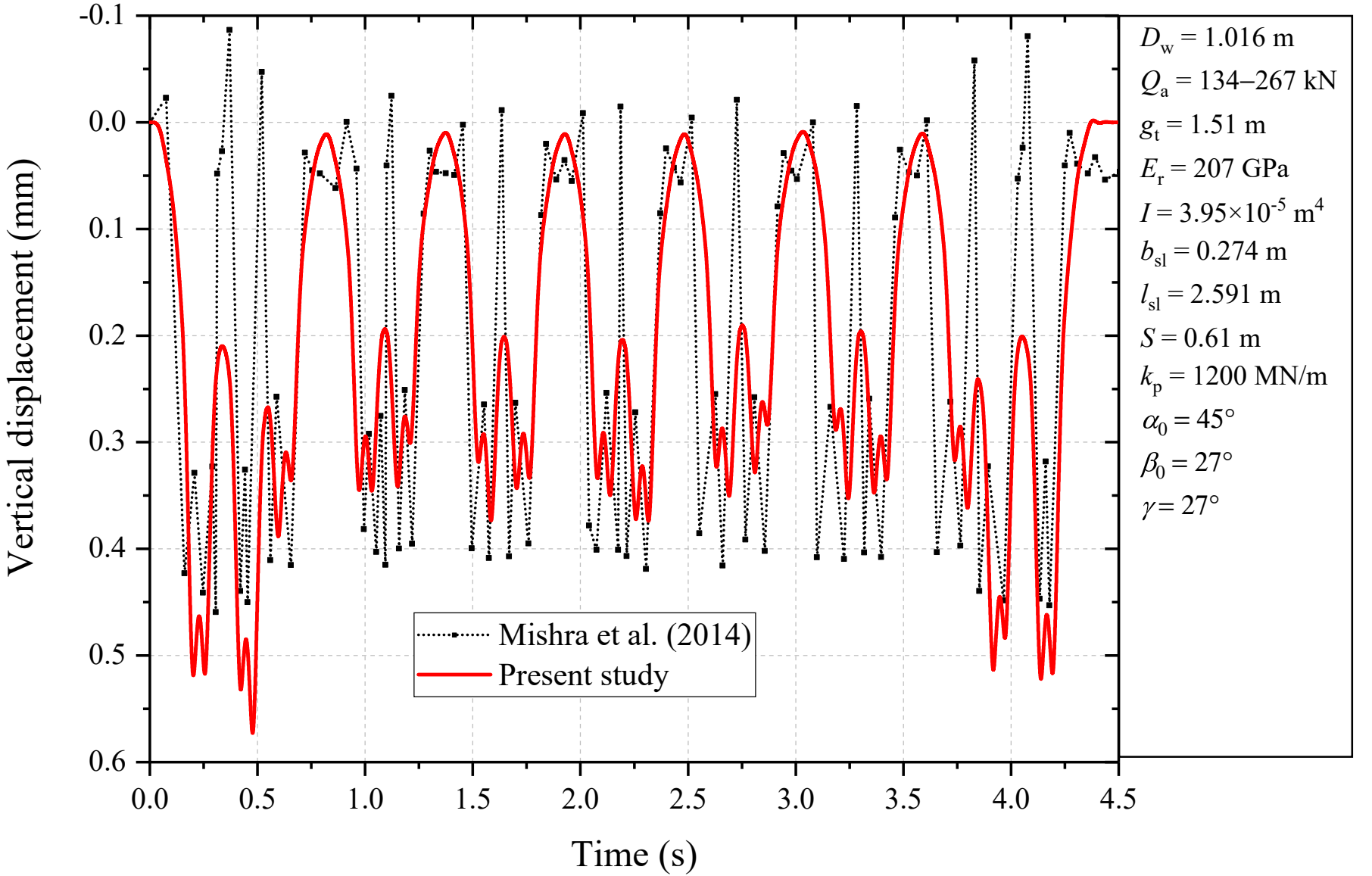
Vertical displacement (mm)
-0.1
0.0
0.1
0.2
0.3
0.4
0.5
0.6
0.0
0.5
1.0
1.5
2.0
2.5
3.0
3.5
4.0
4.5
Time (s)
Mishra et al. (2014)
Present study
D_w = 1.016 m
Q_a = 134–267 kN
g_t = 1.51 m
E_r = 207 GPa
I = 3.95×10^{-5} m^4
b_{sl} = 0.274 m
l_{sl} = 2.591 m
S = 0.61 m
k_p = 1200 MN/m
α_0 = 45°
β_0 = 27°
γ = 27°

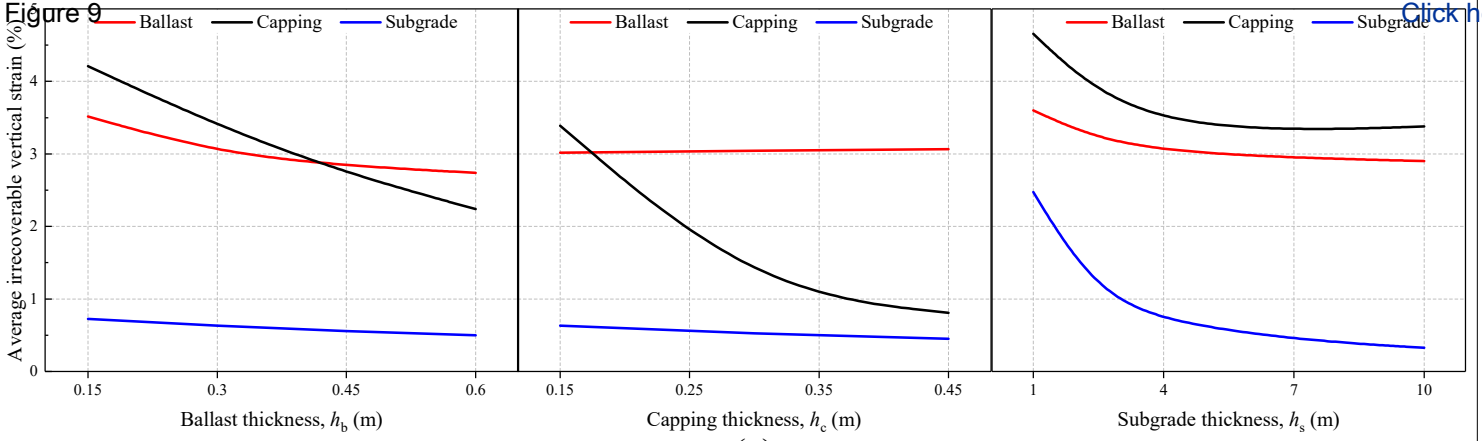

(a)

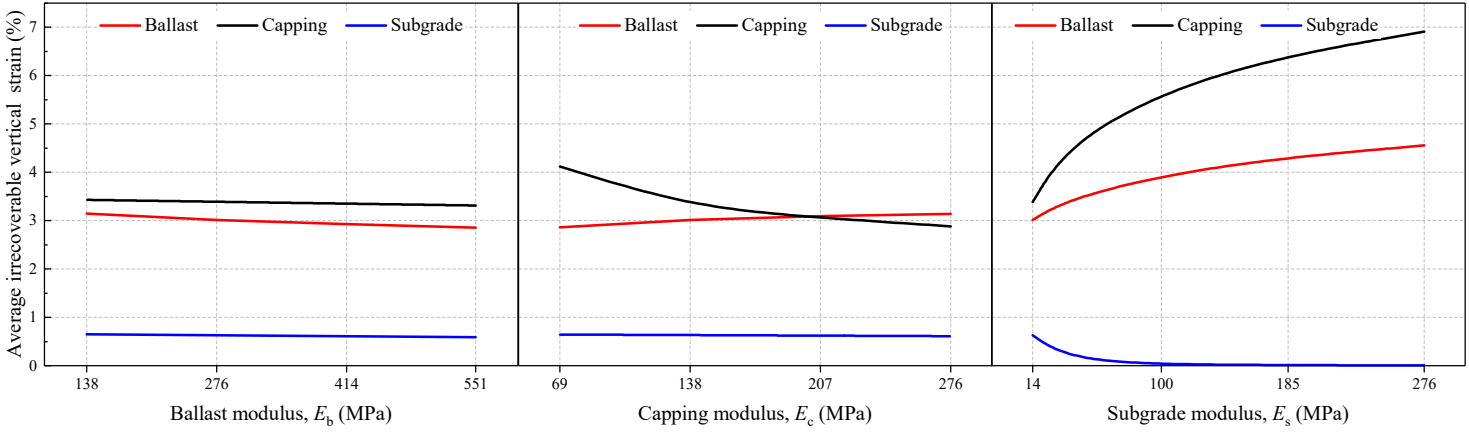

(b)

D_w = 1.016 m
Q_a = 245 kN
i_1 = 0.0058
i_2 = 0.89
g_t = 1.5 m
E_r = 207 GPa
$I = 3.04\times10^{-5}$ m^4
b_{sl} = 0.285 m
l_{sl} = 2.5 m
S = 0.6 m
k_p = 280 MN/m
$\alpha_0 = 45°$
$\beta_0 = 27°$
$\gamma = 27°$
$\varphi'_b = 55°$
$k_1^b = 3.453$
$k_2^b = -2.09$
$k_3^b = 2.745$
$k_4^b = 0.078$
$\varphi'_c = 41°$
$k_1^c = 3.174$
$k_2^c = -4.323$
$k_3^c = 4.588$
$k_4^c = 0.1$
$\varphi'_s = 28°$
$a = 1.1$
$b = 0.16$
$m = 2$
σ_s= 35–600 kPa

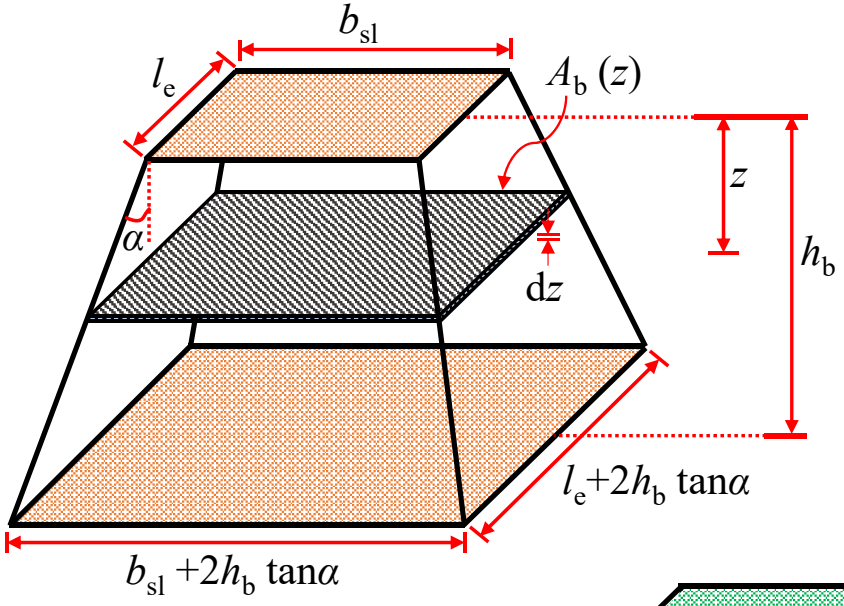

(a) Ballast

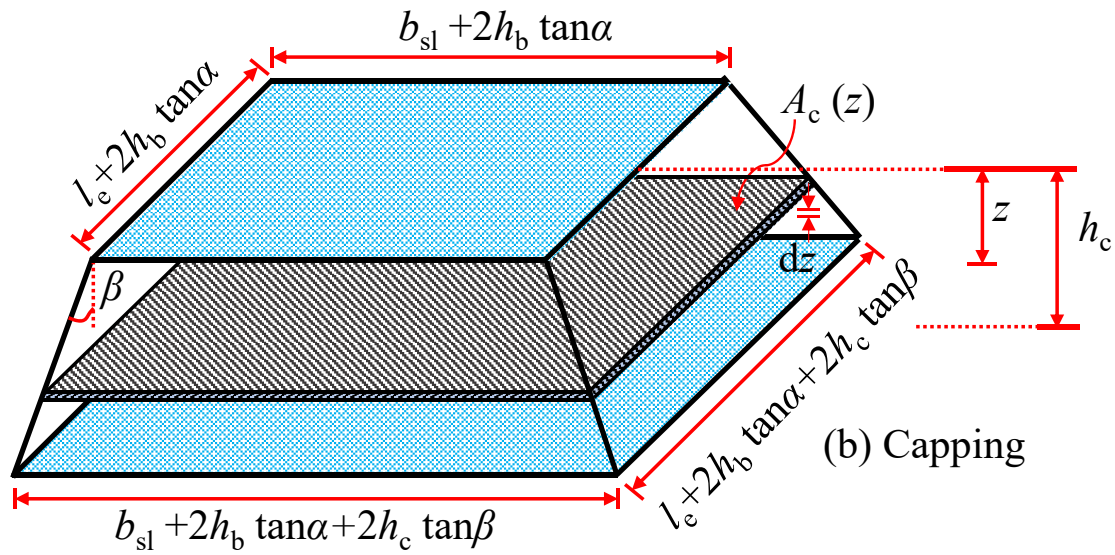

(b) Capping

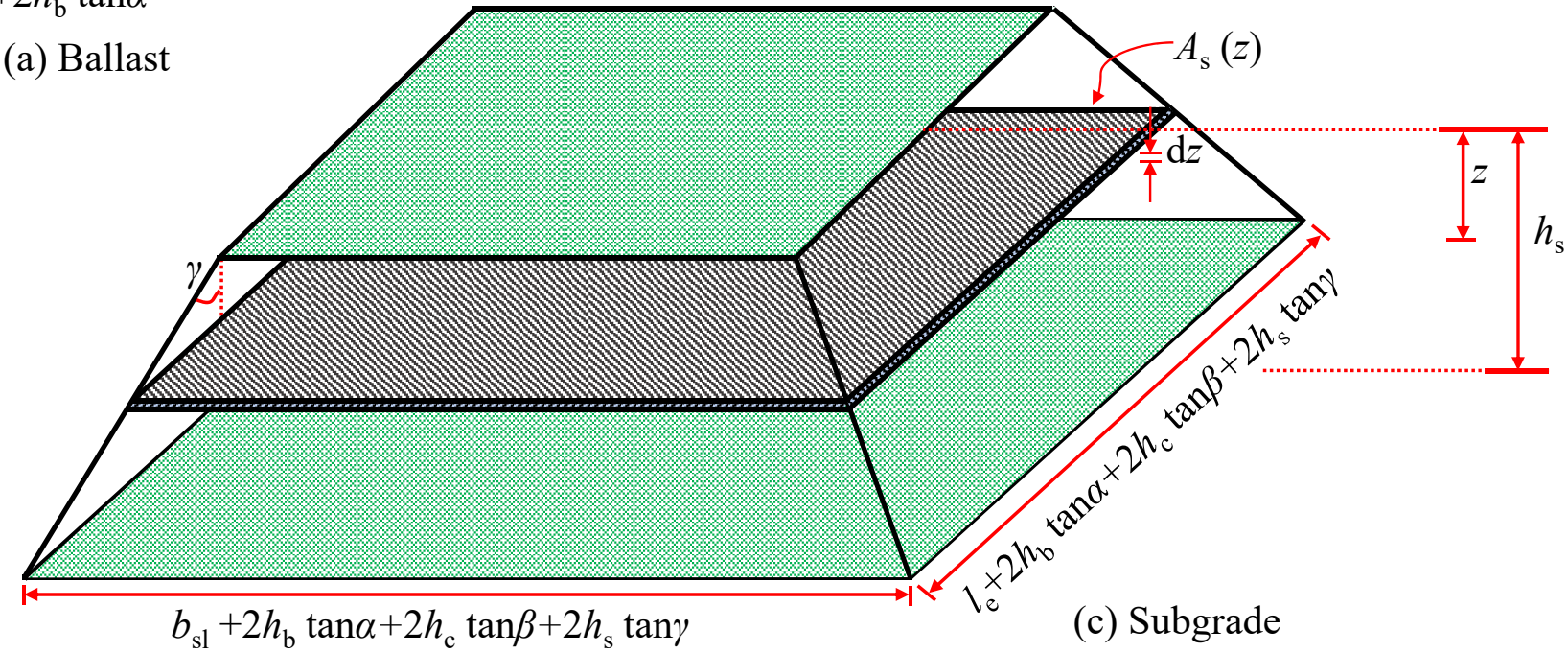

(c) Subgrade